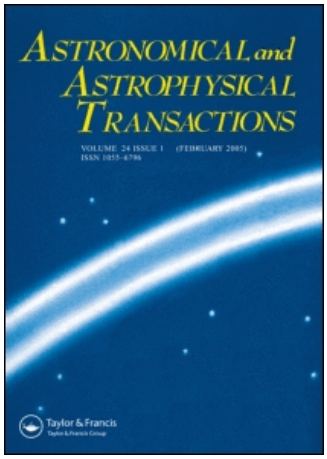

Astronomical & Astrophysical Transactions
The Journal of the Eurasian Astronomical Society
Publication details, including instructions for authors and subscription information:
http://www.informaworld.com/smpp/title~content=t713453505

Simulation of the far infrared emission of blue compact dwarf galaxies

I. Yu. Izotova [a]; Yu. I. Izotov [b]
[a] Astronomical Observatory, Kiev State University, Kiev, Ukraine
[b] Main Astronomical Observatory, Ukrainian AS, Kiev, Ukraine

Online Publication Date: 01 January 1992
To cite this Article: Izotova, I. Yu. and Izotov, Yu. I. (1992) 'Simulation of the far infrared emission of blue compact dwarf galaxies', Astronomical & Astrophysical Transactions, 3:2, 101 - 130
To link to this article: DOI: 10.1080/10556799208230549
URL: http://dx.doi.org/10.1080/10556799208230549

Astronomical and Astrophysical Transactions, 1992, Vol. 3, pp. 101–130
Reprints available directly from the publisher.
Photocopying permitted by license only

SIMULATION OF THE FAR INFRARED EMISSION OF BLUE COMPACT DWARF GALAXIES

I. YU. IZOTOVA[(*),1], YU. I. IZOTOV[2]

[1] *Astronomical Observatory, Kiev State University, Observatorna Str. 3, Kiev, Ukraine 254053,*
[2] *Main Astronomical Observatory, Ukrainian AS, Goloseevo, Kiev, Ukraine 252127*

(Received 16 August 1991; in final form January 8, 1992)

Simulation of the blue compact dwarf galaxies (BCDG) emission in the far infrared range (FIR) and comparison of the predictions with observational data are discussed. Position of the majority of the BCDGs on the FIR color diagrams and on L_{FIR}/L_B vs. L_{FIR} diagrams is shown to be consistently explained basing on the galaxy models comprising an underlying elliptical galaxy with old stars population and several (tens) inhomogeneous star forming regions having different densities. The FIR characteristics of a large number of low-luminosity Markarian galaxies as well as majority of HII galaxies, selected on the basis of the IRAS catalog, are found to be inconsistent with the studied models (i.e. an underlying elliptical galaxy + star formation regions).

KEY WORDS Blue compact dwarf galaxies, far infrared emission, models of.

1. INTRODUCTION

Blue compact dwarf galaxies (BCDGs) belong to the class of low-luminosity irregular galaxies ($M_B \sim -13^m - -17^m$) (Kunth and Sargent, 1983; Kunth, 1988). They are notable for very active star formation which occurs in short starbursts with duration of about 10^7 years. The star formation rate in the starbursts reaches a few solar masses per year (O'Connell *et al.*, 1978). During a starburst, the major portion of the parent galaxy, having the mass of about $\mathfrak{M} \sim 10^6 - 10^7\,\mathfrak{M}_\odot$, represents a supergiant zone of the ionized hydrogen surrounded by a massive HI shell ($\mathfrak{M}_{HI} \approx 0.1 - 0.5\ \mathfrak{M}_{GAL} \approx 10^7 - 10^8\,\mathfrak{M}_\odot$, where $\mathfrak{M}_{GAL}$ is the total galaxy mass) (Kunth, 1988). As indicated by near-infrared observations, an old stellar population surrounds the star formation regions in majority of blue compact dwarf galaxies (Kunth *et al.*, 1988). This provides strong evidence that the observed galaxies now undergo not the first starburst, so that the galaxies have been already enriched by heavy elements due to the evolution of the previous populations. Ultraviolet observations of Fanelli *et al.* (1988) indicate that some blue compact dwarf galaxies have undergone a few starbursts during their evolution.

About the half of the BCDGs from the list of the "most studied" blue compact dwarf galaxies (Kunth and Sevre, 1985) has been already detected by IRAS.

Studies of some blue compact dwarf galaxies show that the heated dust with the temperature about $T_d \sim 40$–60 K, being substantially higher than that in our Galaxy, is the principal source of the BCDGs radiation in the far infrared range (Gondhalekar *et al.*, 1984; Klein *et al.*, 1986; Xu and De Zotti, 1989). The ratio of the dust mass to the gas mass is found to be about 10^2–10^3 times smaller than the heavy elements abundance obtained from optical observations. According to Kunth and Sevre (1985) and Gondhalekar *et al.* (1984), this difference is explained by a possible time delay in the dust production or by a difference in dust properties in BCDGs and the Galaxy.

Simulation of the far-infrared emission for galaxies of different types was a subject of many authors, e.g. Xu and De Zotti (1989), Helou (1986), Crawford and Rowan-Robinson (1986), Rowan-Robinson and Crawford (1986). As a rule, the following sources of the dust heating are considered to be dominant: (1) the background interstellar ultraviolet radiation field produced by the stellar population of the galaxy, usually by the disk component; (2) radiation of hot OB stars embedded in giant HII regions; this radiation component is responsible for the "warm" dust component having the temperature $T_d \sim 40$–60 K; (3) in active galaxies, nonthermal radiation of the nucleus also can contribute into the dust heating.

Blue compact dwarf galaxies have no active nucleus and the dust is heated mainly by hot OB stars in star forming regions and by the old stellar population.

Xu and De Zotti (1989) discuss the simulation of the far infrared radiation of blue compact dwarf galaxies and compare predicted and observed properties of the BCDGs in the far-infrared range. To explain emission of the cold dust component these authors invoke a disk model. However, as shown by Kunth *et al.* (1988), the radial profiles of the surface brightness in the BCDGs are closer to a power law typical of elliptical galaxies than to an exponential law inherent for disk galaxies.

Here we discuss simulations of the far-infrared emission of blue compact dwarf galaxies based on the model considering a BCDG to be similar to an elliptical galaxy. The results are compared with far-infrared observational data.

2. MODEL OF A BLUE COMPACT DWARF GALAXY

A blue compact dwarf galaxy is suggested to contain a supergiant region of ionized hydrogen (the size of about ~1 kpc) excited by a star cluster of the mass about $M_{tot} \sim 10^5$–$10^7\,\mathfrak{M}_\odot$, and an underlying elliptic galaxy having mainly the older population. In the HII region, the gas density is suggested to be constant along the radius (see Crawford and Rowan-Robinson, 1986) and for the elliptical galaxy the gas density is suggested to be a power-law function of the galactocentric radius.

2.1. *Radiation Transfer in the Ionized Hydrogen Region*

Consider scattering of the emission in a homogeneous spherically symmetric medium illuminated by a central source with the monochromatic luminosity L_ν. Here we use the analytic solution of Sobolev (1960). The opacity of the

medium is produced by the dust grains. We introduce the intensity of diffuse radiation I, the volume absorption coefficient α_ν, the probability that a photon survives after scattering λ, and the scattering indicatrix $\chi(\gamma)$ (γ is the angle between propagation directions of the incident and scattered radiation). In terms of these variables, equation of radiation transfer takes the form

$$\cos\vartheta\frac{\partial I(\tau_\nu,\vartheta)}{\partial\tau_\nu}-\frac{\sin\vartheta}{\tau_\nu}\frac{\partial I(\tau_\nu,\vartheta)}{\partial\tau_\nu}=-I(\tau_\nu,\vartheta)+\mathbf{B}(\tau_\nu,\vartheta), \tag{1}$$

where $\tau_\nu=\alpha_\nu r$,

$$\mathbf{B}_\nu=\lambda\int I\chi(\gamma)\frac{\mathrm{d}\omega}{4\pi}+\frac{\lambda\chi(\vartheta)L_\nu}{16\pi^2r^2}\exp(-\tau_\nu). \tag{2}$$

The system of equations (1)–(2) has been solved using an approximate method of Sobolev (1960), in the framework of which scattering of the first order is taken into account exactly and the higher-order scattering is included approximately, with neglecting other terms in the series expansion of the scattering indicatrix in the Legendre polynomials except the lower. The approximate solution of the system of equations (1)–(2) yields the following result for the mean diffuse emission flux $\bar{H}_\nu$ along the radius vector (for simplicity, the subscript ν is omitted):

$$\begin{aligned}\tau^2(3-\lambda x_1)\bar{H}(\tau)&=x_1\lambda A\exp(-\tau)+(1+k\tau)\exp(-k\tau)\\&\times\left\{C_1-\lambda A\frac{3+(1-\lambda)x_1}{2k}[Ei(1-k)\tau-Ei(1-k)\tau_0]\right\}\\&+(1-k\tau)\exp(k\tau)\left\{C_2+\lambda A\frac{3+(1-\lambda)x_1}{2k}[Ei(1+k)\tau-Ei(1+k)\tau_0]\right\},\end{aligned} \tag{3}$$

where

$$Ei(\tau)=\int_\tau^\infty\exp(-x)\frac{\mathrm{d}x}{x},\qquad A=\frac{La^2}{16\pi^2},$$

$$k^2=(3-\lambda x_1)(1-\lambda),\qquad x_1=\frac{3}{2}\int_0^\pi\chi(\gamma)\cos\gamma\sin\gamma\,\mathrm{d}\gamma,$$

and C_1 and C_2 are constants of integration determined by the following boundary conditions: $\bar{H}\times\tau^2\to 0$ for $\tau\to 0$ and $\bar{H}=\frac{1}{2}\times I$ for $\tau=\tau_0$. Eq. (3) gives the emission flux $\bar{H}_\nu$ at any point.

2.2. *The Energy Spectral Distribution of the Central Star Cluster*

We adopt a power-law initial mass function (IMF) with the Salpeter slope, $\beta=2.35$. We also use the value $\beta=2.0$ following Matteucci and Tosi (1985) who note that the mass function for higher-mass stars in blue compact dwarf galaxies in a number of cases has, probably, a smaller slope than Salpeter's IMF. The number of stars per mass interval $(m, m+\mathrm{d}m)$ is given by

$$\mathrm{d}N=Cm^{-\beta}\,\mathrm{d}m. \tag{4}$$

The value of the constant C can be obtained using the total mass of the star cluster $M_{\rm tot}$:

$$M_{\rm tot} = C \int_{m_l}^{m_u} m^{-\beta}\, {\rm d}m, \tag{5}$$

where m_l and m_u are the lower and upper mass cutoffs, which are chosen as $1\,\mathfrak{M}_\odot$ and $120\,\mathfrak{M}_\odot$, respectively (Sramek and Weedman, 1986; Campbell *et al.*, 1986). Then the total monochromatic stellar luminosity of the HII region is the following:

$$L_{\rm HII}(\nu) = C \int_{m_l}^{m_u} L_*(m, \nu) m^{-\beta}\, {\rm d}m, \tag{6}$$

where

$$L_*(m, \nu) = 4\pi R_*^2(m) \pi \mathbf{B}\{T_*(m)\} \tag{7}$$

is the monochromatic luminosity of the star of the mass m, $R_*(m)$ is the star radius, $\mathbf{B}_\nu$ is Plank's function, T_* is the effective temperature of the star. The functions of stellar mass $\mathbf{B}_\nu = \mathbf{B}_\nu[T_*(m)]$ and $R_* = R_*(m)$ are approximated using results of Thompson (1984) and Avedisova (1979).

2.3. *The Grain Model and the Temperature of the Warm Component*

The dust is assumed to be a mixture of graphite and silicate grains (see Xu and De Zotti, 1989 for motivation of this choice for blue compact dwarf galaxies). The dust grain optical properties in the ultraviolet and visible ranges (such as the mean cosine of the scattering angle and the albedo) which depend on the wavelength, have been taken from Bruzual *et al.* (1988). Following Mathis *et al.* (1977), we adopt the dust grains size distribution in the form:

$$\rho(a_{\rm d}) \sim a_{\rm d}^{-3.5} \tag{8}$$

for $50\ \text{Å} \leq a_{\rm d} \leq 2500\ \text{Å}$.

The heavy elements abundance in blue compact dwarf galaxies varies in a wide range from $\frac{1}{80}$ to $\frac{1}{2}$ in the solar-value units. The relative content of the dust in these galaxies should be expected to vary substantially as well.

The ratio of the dust number density to the hydrogen number density,

$$b = \frac{n_{\rm d}}{n_{\rm H}}, \tag{9}$$

can be found from the assumption that about the half of the heavy elements mass is within the dust grains:

$$\frac{M_{\rm d}}{M_{\rm H}} = \tfrac{1}{2} Z = \frac{\int \bar{n}_{\rm d} m_{\rm d}\, {\rm d}a_{\rm d}}{n_{\rm H} m_{\rm H}}, \tag{10}$$

where

$$\bar{n}_{\rm d} = {\rm const} \times a_{\rm d}^{-3.5} \tag{11}$$

is the number of the dust grains of the size $a_{\rm d}$ per unit size interval,

$$m_{\rm d} = \tfrac{4}{3} \pi a_{\rm d}^3 \rho_{\rm d} \tag{12}$$

is the mass of an individual dust grain, $\rho_d = 2\ \mathrm{g/cm^3}$, m_H is the hydrogen atom mass, Z is the heavy element mass fraction.

The total dust grain number density is equal to

$$n_d = \mathrm{const} \int a_d^{-3.5}\, da_d. \tag{13}$$

Then Eqs. (9), (10) and (13) yield

$$b = 3.5 \times 10^{-10} z, \tag{14}$$

where

$$z = \frac{Z}{Z_\odot}.$$

The absorption efficiency for optical and UV photons is taken to be

$$Q_a(\lambda) = \frac{\chi_\lambda}{1+\chi_\lambda}, \tag{15}$$

where $\chi_\lambda = (2\pi a_d)/\lambda$, and a_d and λ are measured in cm.
Then the total optical depth at the wavelength λ is given by

$$\begin{aligned} d\tau_\lambda &= dr \int \tilde{n}_d \pi a_d^2 Q_a(\lambda)\, da_d \\ &= 2.4364 \times 10^{-24}\, dr n_H z \lambda^{-1/2} \{\arctan(\sqrt{\lambda/(2\pi a_{d,\min})}) \\ &\quad - \arctan(\sqrt{\lambda/(2\pi a_{d,\max})})\}, \end{aligned} \tag{16}$$

where $a_{d,\min} = 50$ Å, $a_{d,\max} = 2500$ Å.

The energy fraction absorbed by the dust grains in the size interval $(a_d, a_d + da_d)$ is equal to $d\tau_{\lambda,a}/d\tau_\lambda$, where

$$\begin{aligned} d\tau_{\lambda,a} &= 2.4364 \times 10^{-24}\, dr n_H z \lambda^{-1/2} \{\arctan(\sqrt{\lambda/(2\pi a_d)}) \\ &\quad - \arctan(\sqrt{\lambda/(2\pi(a_d + da_d))})\} \end{aligned} \tag{17}$$

is the optical depth produced by dust grains of the sizes ranging from a_d to $a_d + da_d$.

Assuming that the radiation absorbed by the dust is reemitted into the far infrared range, one can determine, from the energy balance equation, the dust temperature as a function of the distance to the center of the star forming region.

Consider now equation of energy balance. The energy absorbed by dust grains within the size interval $(a_d, a_d + da_d)$ in a layer of the thickness $\Delta r = r_j - r_{j-1}$ is as follows:

$$E_{ABS}(a_d) = \int E_{SUM}(\lambda) \frac{d\tau_{\lambda,a}}{d\tau}\, d\lambda, \tag{18}$$

where $E_{SUM}(\lambda)$ is total energy absorbed by the dust grains of all sizes at the wavelength λ. Having solved the transfer equation using Sobolev's method and having calculated the mean diffuse flux $\bar{H}_\lambda$ as a function of the distance to center (see (3)) and having also taken into account the direct incident radiation, one can find $E_{SUM}(\lambda)$, the total energy absorbed at the wavelength λ by dust grains of all sizes within the layer of the thickness $\Delta r = r_j - r_{j-1}$.

The energy emitted by dust grains of the sizes $(a_d, a_d + da_d)$ in the far infrared range is

$$E_{FIR} = n_H A(a_d) 4\pi a_{d3}^{24} \pi r^2 \, dr \int \varepsilon_\nu Q_\nu \, d\nu, \tag{19}$$

where

$$A(a_d) = \frac{n_d(a_d, a_d + da_d)}{n_H}, \tag{20}$$

$$\varepsilon_\nu = \pi \mathbf{B}_\nu [T_d(a_d)], \tag{21}$$

and Q_ν is the absorption efficiency for far infrared photons. Following Xu and De Zotti (1989), we assume that

$$Q_\nu = 0.065 \, a_d \lambda^{-1.7}. \tag{22}$$

Using results of Fitt *et al.* (1989), the integral in Eq. (19) can be evaluated as follows:

$$\int \varepsilon_\nu Q_\nu \, d\nu = \int F_\nu(T_d) \, d\nu = 0.115 \left(\frac{\pi k T_d(a_d)}{h} \right)^{5.7}. \tag{23}$$

The temperature of the dust grains of each size as a function of the distance r to center follows from the equation

$$E_{ABS}(a_d) = E_{FIR}(a_d), \tag{24}$$

which allows to calculate predicted flux densities S_{12}, S_{25}, S_{60}, S_{100} in the far infrared range. To compare the results with observations, the predicted flux densities were convolved with IRAS's response function (IRAS Catalogs and Atlases. Explanatory, 1985). The total far-infrared luminosity of the warm component in the HII region is given by

$$\frac{L_{FIR}}{L_\odot} = 3.89 \times 10^5 (2.58 S_{60}(Jy) + S_{100}(Jy)) \times D^2, \tag{25}$$

where D is distance in Mpc.

2.4. *Polycyclic Aromatic Hydrocarbon (PAH) Molecules*

As noted by some authors, e.g. Xu and De Zotti (1989), in order to explain the emission observed at $\lambda < 20 \, \mu m$, the presence of the very small dust particles heated to high temperatures by a single UV or optical photon is required. These small particles were identified as polycyclic aromatic hydrocarbon (PAH) molecules. As shown by Puget *et al.* (1985) and Philips and Roche (1984), PAH molecules contribute mainly to the emission at $\lambda\lambda$ 7.8, 8.8 and 11.3–11.9 μm. Therefore, we assume that the whole energy absorbed by PAH molecules is reemitted in the 12 μm band. PAH molecules are assumed to be present, in different proportions, both in HII regions and in the elliptical galaxy.

Following Puget *et al.* (1985), we adopt the range of sizes for PAH molecules to extend from $a_{PAH}^{min} = 4$ Å to $a_{PAH}^{max} = 15$ Å. The absorption efficiency in the UV

range is taken to be

$$\sigma_{\mathrm{PAH}} = \frac{3.2 \times 10^{-6}}{\lambda} a_{\mathrm{PAH}}^2. \tag{26}$$

The number density of PAH molecules can be estimated as follows. The value of A_{PAH} is obtained by extrapolation of the grain size distribution to the size range of the PAH molecules:

$$A_{\mathrm{PAH}} = \frac{n_{\mathrm{PAH}}}{n_{\mathrm{H}}} = 1.43 \times 10^{-7} z. \tag{27}$$

However, in reality this quantity can be very inhomogeneous because in HII regions the PAH molecules can be destroyed easier than the dust grains which have larger size. To account for this effect, we introduce the factor **X**. The value $\mathbf{X} = 1$ is consistent with A_{PAH} as given by Eq. (27). In the UV and optical ranges, the optical depth due to the PAH molecules is

$$\Delta\tau_{\mathrm{PAH}} = \Delta r \int \sigma_{\mathrm{PAH}}\, \mathrm{d}n_{\mathrm{PAH}}. \tag{28}$$

Then the energy fraction absorbed by PAH molecules at the wavelength λ is equal to

$$\delta = \frac{\Delta\tau_{\mathrm{PAH}}}{\Delta\tau_{\mathrm{PAH}} + \Delta\tau_{\mathrm{DUST}}}, \tag{29}$$

while the total energy absorbed by PAH molecules is δE_{SUM}, where E_{SUM} is the total energy absorbed within the layer $(r, r + \mathrm{d}r)$.

As mentioned above, we assume that the energy absorbed by PAH molecules is reemitted only in the 12 μm band. To conclude this section, we note again that the IRAS response function has been taken into account in our calculations.

2.5. *A Model for the Cold Component*

The cold component is modelled as emission of the dust heated by the general interstellar radiation field.

As we already noted, the surface brightness profiles in the outer regions of blue compact dwarf galaxies vary as power-laws (Kunth *et al.*, 1988) being similar to those in elliptical galaxies. For elliptical galaxies, the emissivity distribution has the form (Jura, 1982)

$$\varepsilon = \varepsilon_0 \quad \text{for } r \leq r_0,$$
$$\varepsilon = \varepsilon_0 \left(\frac{r_0}{r}\right)^3 \quad \text{for } r > r_0, \tag{30}$$

where r_0 is the core radius of the elliptical galaxy and ε_0 is the emissivity at $r = r_0$. The resulting intensity of radiation at the radius $r > r_0$ is then as follows (Jura, 1982):

$$I = \frac{\varepsilon_0}{16\pi} \frac{r_0^3}{r} \left[\frac{2}{r_0} \ln\left(\frac{r + r_0}{r - r_0}\right) + \frac{2}{r} \ln\left(\frac{r^2 - r_0^2}{r_0^2}\right)\right]. \tag{31}$$

For elliptical galaxies, r_0 is usually taken to be about $r_0 \approx 0.01R$ (R being the galaxy radius) and the emissivity at the radius r_0 at the wavelength $\lambda = 5500$ Å (V band) is equal to $\varepsilon_0 = 1.2 \times 10^{-35}$ erg cm^{-3} s^{-1} Hz^{-1}, corresponding to the surface brightness of 16 V mag arcsec^{-2}.

According to Kunth *et al.* (1988), blue compact dwarf galaxies have $r_0 \approx 0.1R$ and the surface brightness of the galaxy central core is equal to about 19–20 V mag arcsec^{-2}. These values of r_0 and surface brightness have been taken into account in calculations of the cold component contribution into the BCDG dust heating.

The temperature of the cold dust component has been obtained from the energy balance equation written for an optically thin case (and for the dust grain with size a_d):

$$4\pi I_{5500}(r) \int \frac{I_\lambda(r)}{I_{5500}(r)} \pi a_d^2 Q_\lambda \, d\lambda = 4\pi a_d^2 \int \mathbf{B}_\lambda(T_d) Q_{FIR}(\lambda) \, d\lambda, \tag{32}$$

where $I_{5500}(r)$ can be obtained from Eq. (31), the absorption efficiency Q_λ in the optical range has been calculated using Eq. (15) which was also used in the case of the HII region. The spectral distribution $I_\lambda(r)/I_{5500}(r)$ is taken from Coleman *et al.* (1980) for the old stellar population in the galaxy. This value is assumed to be independent of r. However, we should note that in the outer parts of the BCDGs the colors become redder with the galactocentric distance.

Having obtained the dust grain temperature, for the grain size a_d, as a function of the distance to the center, and having taken into account the size distributions for the grains and PAH molecules as it was done in Sections II.3 and II.4, one can find the old-component fluxes at $\lambda\lambda$ 12, 25, 60 and 100 μm using the assumption of the black body radiation.

3. RESULTS AND CONFRONTATION OBSERVATIONS

The model calculations of the blue compact dwarf galaxy far-infrared properties have been carried out upon adopting the following parameters: the total stellar mass of the star forming region is assumed to be $M_{tot} = 10^5\,\mathfrak{M}_\odot$, $10^6\,\mathfrak{M}_\odot$ and $10^7\,\mathfrak{M}_\odot$; the lower stellar mass cutoff is taken as $m_l = 1\,\mathfrak{M}_\odot$; in order to account for the evolution effects in the far-infrared properties of the blue compact dwarf galaxies, the upper mass cutoff is varied in the range $m_u = 20 - 120\,\mathfrak{M}_\odot$. According to Dufour and Hester (1990), the mean gas density n_H in the ionized hydrogen region of the BCDGs is equal to about 10 cm^{-3}, and the heavy element abundance varies from $\frac{1}{2} Z_\odot$ to $\frac{1}{77} Z_\odot$ (Kunth and Sargent, 1983; Izotov *et al.*, 1990) (see Section 2.3). The optical depth of the star forming region in the ultraviolet and visible ranges is determined with intersection of $n_H z$, where $z = Z/Z_\odot$ (n_H being the gas number density). For $n_H z$, discrete values 0.03, 0.1, 1.0, 3.0 have been taken, which cover the whole range of the n_H and Z variations in the blue compact dwarf galaxies. The dust is assumed to contain about the half of the heavy elements content. The size of the region in which the gas heating by the young stars of the HII region is substantial, depends on the parameters adopted being on average about 100 pc.

In order to evaluate the contribution of the old stellar population, we adopt the total size of the underlying elliptical galaxy to be either 2 or 5 kpc, the intensity distribution is assumed to be given by Eq. (31), and the gas density distribution is taken to be a power law $\sim r^{-\gamma}$ with $\gamma = 2$ or $\gamma = 3$. The gas density n_H^0 at $r = r_0$ is calculated from the assumption that the total neutral hydrogen mass is $M_{HI} = 1 \times 10^7\,\mathfrak{M}_\odot$ or $1 \times 10^8\,\mathfrak{M}_\odot$. Thus, n_H^0 depends on the adopted total size, the neutral hydrogen mass and the adopted power-law index.

3.1. *Distribution of the Dust Temperature in the Star Forming Region and in the Elliptical Galaxy*

Figure 1 (a, b, c) and Figure 2 show the distribution of the T_d temperature along the radius in the star forming region and in the elliptical galaxy, respectively. As far as the star forming region is opaque in the UV and visible ranges, the T_d temperature distribution depends on the adopted $n_H z$ values. The dust temperature decreases along the radius at larger slope when $n_H z$ is larger. In the central layers of the star forming region, the dust temperature reaches the values of the order of 100 K and decreases to 10–20 K (becoming typical of the interstellar medium) at the boundary of the star forming region. The gradient of T_d probably can explain the small value of the ratio of the dust mass to the gas mass observed in the BCDGs, which tends to be about two orders of magnitude smaller than the

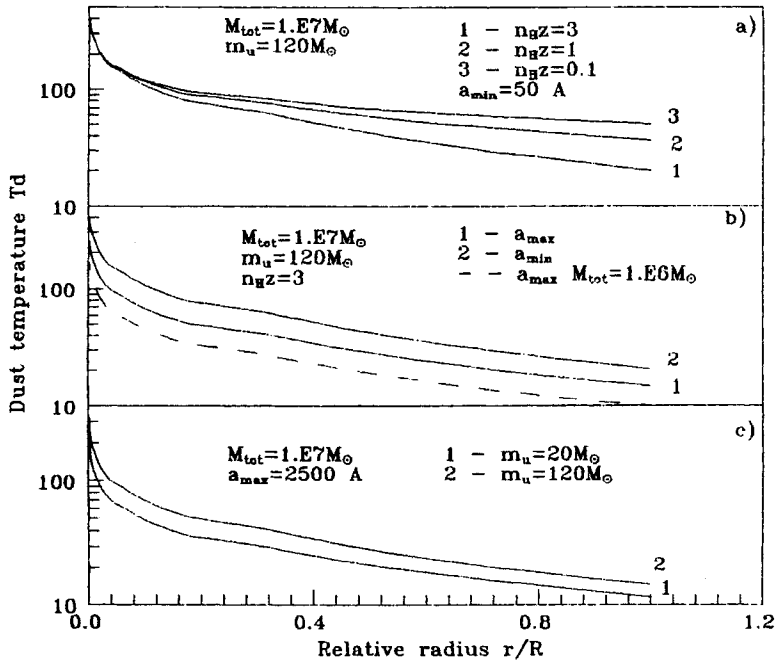

Figure 1 The dust temperature T_d as a function of the relative radius r/R in the star forming region for (*a*) various values of $n_H z$; (*b*) for various sizes of dust grains; (*c*) for various values of the upper mass cutoff m_u.

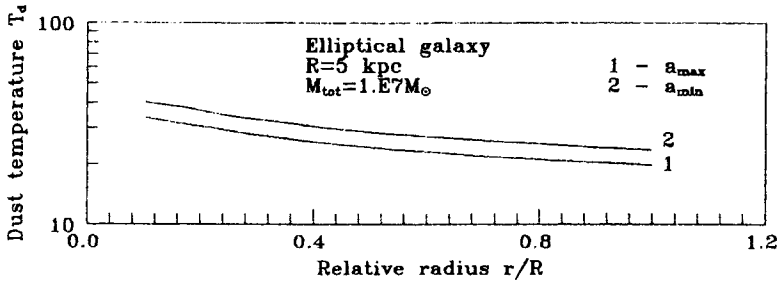

Figure 2 The dust temperature T_d distribution along the relative radius r/R in the underlying elliptical galaxy.

heavy element abundance obtained from optical observations. The dust emissivity strongly depends on T_d (see Eq. (23)). Therefore, the central layers of the star forming region with the radius $r \sim 200$–300 pc produce the main contribution into the galaxy radiation in the far infrared range whereas the gas mass is determined from the 21 cm observations of the whole galaxy of the size $\sim(1-2)\times 10^3$ pc. Therefore, in order to explain the difference in the heavy element abundance obtained from optical observations on the one hand and from the radio and far-infrared observations on the other hand, some additional assumptions are not required, this conclusion being in contradiction to those of Gondhalekar *et al.* (1984) and Klein *et al.* (1986).

The value of T_d in an elliptical galaxy is substantially lower than that in the star forming region (Figure 2) being typical of a diffuse component powered by the general interstellar radiation.

Variations in the upper stellar mass cutoff (m_u is taken to range from $20\,\mathfrak{M}_\odot$ to $120\,\mathfrak{M}_\odot$) in the initial mass function (IMF) of the star formation region only weakly affect the average dust temperature T_d (Figure 1c). The IMF with the slope $\beta = 2.0$ leads the dust temperature to be somewhat higher than that for the IMF with the slope $\beta = 2.35$ because of a larger fraction of high-luminosity stars in the former case.

The principal observational parameters which could be explained with the models proposed in the present paper are as follows: the color indices of the blue compact dwarf galaxies S_{12}/S_{25}, S_{25}/S_{60} and S_{60}/S_{100}; the luminosity in the far infrared range L_{FIR}; and the L_{FIR}/L_B ratio (L_B being the galaxy luminosity in the B band).

The samples of the best studied blue compact dwarf galaxies from Kunth and Sevre (1985), Klein *et al.* (1984) and the sample of low-luminosity Markarian galaxies ($M_B > -18^m$) from Markarian *et al.* (1989) are shown in the Table 1 and Table 2, respectively. In addition, in Table 3 we give the data for HII galaxies (de Grijp *et al.*, 1987) which were selected from the IRAS catalog and observations in the visible range. In the latter sample only the galaxies detected in all IRAS bands (12 μm, 25 μm, 60 μm, and 100 μm) were chosen. These samples are used for comparison of the observed parameter values with those predicted by model calculations.

3.2. *A Model Consisting of an Isolated Star Forming Region*

Suppose that a blue compact dwarf galaxy is an isolated star forming region of uniform density (as the simplest case). This model is also suitable for those

Table 1 The sample of blue compact dwarf galaxies from Kunth and Sevre (1985) and Klein *et al.* (1984)

	Galaxy	S_{12}	S_{25}	S_{60}	S_{100}	*d, Mpc*	M_B
1	2	3	4	5	6	7	8
1.	NGC 1522	<0.30	<0.30	0.89	1.44	9.6	−16.0
2.	Mkn 1089	<0.30	0.70	4.00	5.43	53.0	−19.8
3.	II Zw 40	0.46	1.92	6.49	5.68	10.1	−13.7
4.	Mkn 8	<0.30	0.41	2.37	3.82	41.0	−18.9
5.	He 2-10	1.10	6.55	23.80	25.70	8.7	−16.7
6.	Mkn 1236	<0.30	<0.30	2.28	4.85	24.5	−18.5
7.	Mkn 710	<0.30	<0.50	2.66	4.18	–	–
8.	Tol 3	<0.30	<0.80	4.91	6.24	11.6	−16.5
9.	Mkn 33	<0.30	0.98	4.73	5.25	21.6	−18.2
10.	Mkn 35	<0.30	0.93	5.13	6.37	14.5	−17.3
11.	Mkn 162	<0.30	0.35	1.31	1.58	86.1	−20.1
12.	NGC 3690	3.73	21.60	105.40	110.00	40.8	−20.6
13.	Mkn 1304	<0.30	0.86	3.81	4.34	73.0	−19.8
14.	VV 523	<0.30	<0.30	2.53	4.64	44.3	−17.2
15.	Mkn 432	<0.30	0.42	3.58	6.44	45.6	−19.2
16.	Pox 36	<0.30	<0.50	0.83	1.23	14.9	−16.9
17.	NGC 4214	0.40	1.76	14.24	24.75	6.4	−17.9
18.	IC 3258	<0.40	<0.30	0.48	0.96	21.2	−17.8
19.	NGC 4670	<0.30	<0.30	2.41	3.84	12.1	−17.3
20.	NGC 4861	<0.30	<0.40	1.83	2.29	11.0	−16.3
21.	Tol 35	<0.30	<0.30	1.82	3.43	22.7	−16.7
22.	II Zw 70	<0.30	<0.30	0.71	1.41	17.6	−16.3
23.	I Zw 123	0.40	0.30	0.44	1.00	10.4	−14.5
24.	Mkn 296	<0.30	<0.30	0.61	1.36	65.3	−18.1
25.	NGC 6764	0.38	1.34	6.41	11.47	32.0	–
26.	T1924-416	<0.40	0.51	1.61	1.34	12.0	–
27.	II Zw 102	0.58	1.03	8.98	18.28	105.0	−19.7
28.	IV Zw 149	<0.30	0.55	5.18	6.71	–	–
29.	III Zw 107	<0.30	0.33	1.49	1.73	73.7	−19.3
30	NGC 7714	0.50	2.81	11.10	10.90	40.0	−19.8

galaxies whose star forming regions have the luminosities in the far infrared (FIR) and visible ranges that exceed the luminosities of the old star population.

Figure 3 shows relation between the colors in the FIR range for the models of the star forming region (SFR) with the total stellar mass of $M_{\text{tot}} = 10^6\,\mathfrak{M}_\odot$ for various values of the upper stellar mass cutoff, $m_u = 20 - 120\,\mathfrak{M}_\odot$, and different choices of $n_{\text{H}}z$ noted in Figure 3a. In Figure 3 and in all subsequent figures, the observed colors of galaxies are given only for the sake of comparison (the BCDGs from Kunth and Sevre (1985) and Klein *et al.* (1984) are denoted by circles, Markarian galaxies from Markarian *et al.* (1989) are shown by asterisks, HII galaxies from de Grijp *et al.* (1987) are indicated by triangles). As follows from Figure 3, positions of the bulk of galaxies in the diagrams $\log(S_{60}/S_{100})$ vs. $\log(S_{12}/S_{25})$ and $\log(S_{60}/S_{100})$ vs. $\log(S_{25}/S_{60})$ are consistently explained with the model of the isolated star forming region. But such models do not cover the whole range of the colors observed. To explain the color characteristics of the galaxies in the diagram $\log(S_{25}/S_{60})$ vs. $\log(S_{12}/S_{25})$ (Figure 3a), one probably has

Table 2 The sample of low luminosity Markarian galaxies from Markarian *et al.* (1989)

	FBS number	*z*	S_{12}, *Jy*	S_{25}, *Jy*	S_{60}, *Jy*	S_{100}, *Jy*	*d*, *Mpc*	M_B
1	2	3	4	5	6	7	8	9
1.	577	0.0125	–	0.35	1.12	1.21	50	−18.2
2.	968	0.0149	–	0.98	0.78	1.63	59.6	−18.6
3.	970	0.0083	–	<0.28	0.60	1.27	33.2	−17.4
4.	563	0.0169	–	0.33	0.70	1.42	67.6	−18.9
5.	980	0.0162	–	<0.25	0.54	1.77	64.8	−18.6
6.	990	0.0159	–	<0.25	0.67	1.34	63.6	−18.8
7.	1003	0.0101	–	<0.32	0.59	1.26	40.4	−18.9
8.	1026	0.0126	–	<0.45	1.40	3.04	50.4	−18.8
9.	1031	0.0082	–	<2.99	0.65	1.11	32.8	−17.4
10.	1177	0.0227	–	<0.25	0.80	1.71	90.8	−18.5
11.	1039	0.0064	–	0.40	1.48	1.57	25.6	−16.8
12.	1043	0.0081	–	0.30	1.54	2.89	32.1	−18.8
13.	370	0.0030	–	<0.31	1.12	2.91	12.0	−17.6
14.	1063	0.0048	–	0.43	2.99	4.76	19.2	−18.7
15.	1069	0.0047	–	0.26	1.36	1.90	18.8	−17.2
16.	603	0.0081	0.50	2.38	12.60	15.30	32.4	−18.4
17.	1075	0.0072	–	<0.26	0.76	1.65	28.8	−18.1
18.	1078	0.0135	–	<0.37	0.54	1.14	54.0	−18.5
19.	1080	0.0023	–	<0.25	1.46	3.65	9.2	−17.1
20.	615	0.0152	–	<0.25	0.70	1.13	60.8	−18.4
21.	1085	0.0160	–	0.25	1.04	2.50	64.0	−18.5
22.	1093	0.0141	0.34	1.32	9.15	12.30	56.4	−18.8
23.	71	0.0009	–	0.73	3.28	4.38	3.6	−16.7
24	13	0.0050	–	<0.25	0.48	1.00	20.0	−17.5
25.	86	0.0015	–	0.42	3.15	6.26	6.0	−17.6
26.	15	0.0219	–	<0.25	0.59	1.33	87.6	−18.1
27.	92	0.0130	0.25	0.38	2.50	3.72	52.0	−19.0
28.	1221	0.0108	–	<0.30	0.84	1.59	43.2	−17.6
29.	93	0.0180	–	0.49	1.58	1.41	72.0	−19.0
30.	19	0.0141	–	<0.25	0.56	1.00	56.4	−18.5
31.	1230	0.0048	–	<0.35	1.12	1.55	19.2	−17.3
32.	394	0.0087	–	<0.35	1.28	1.76	34.8	−18.8
33.	399	0.0160	–	<0.25	1.02	1.48	64.0	−17.9
34.	1418	0.0023	–	<0.34	0.56	1.21	9.2	−16.6
35.	404	0.0039	0.66	1.35	11.70	23.20	15.6	−15.8
36.	710	0.0039	–	0.47	2.66	4.18	15.6	−17.8
37.	416	0.0041	–	<0.32	0.58	1.13	16.4	−16.2
38.	157	0.0050	–	<0.27	0.62	1.30	20.0	−17.8
39.	163	0.0250	–	<0.28	0.76	1.53	100.0	−17.8
40.	731	0.0040	–	0.69	2.99	4.58	16.0	−17.9
41.	1443	0.0022	–	0.25	1.22	2.70	8.8	−17.4
42.	171	0.0010	3.73	21.60	105.00	110.00	4.0	−16.5
43.	743	0.0029	–	<0.31	1.48	1.77	11.6	−17.5
44.	1305	0.0100	–	<0.27	0.94	1.67	40.0	−17.8
45.	186	0.0020	–	<0.25	1.17	2.41	8.0	−16.6
46.	750	0.0018	–	<0.89	0.46	1.00	7.2	−14.1
47.	190	0.0030	0.25	0.44	2.65	5.23	12.0	−17.5
48.	1309	0.0054	–	<0.31	1.13	2.00	21.6	−17.0
49.	195	0.0050	–	0.27	1.78	2.52	20.0	−17.5
50.	197	0.0080	–	<0.25	0.57	1.01	32.0	−18.1
51.	1315	0.0021	–	<0.26	0.71	1.96	8.4	−13.4
52.	49	0.0034	–	<0.32	0.74	1.00	13.6	−16.4
53.	206	0.0030	–	0.30	1.20	1.70	12.0	−15.2
54.	1326	0.0033	–	<0.44	0.97	2.79	13.2	−17.3
55.	773	0.0026	–	<0.25	0.60	2.06	10.4	−16.2

Table 2 (*Continued*)

	FBS number	*z*	S_{12}, *Jy*	S_{25}, *Jy*	S_{60}, *Jy*	S_{100}, *Jy*	*d*, *Mpc*	M_B
1	2	3	4	5	6	7	8	9
56.	1333	0.0028	0.37	0.66	3.25	5.18	11.2	−16.0
57.	223	0.0040	–	<0.25	0.74	1.18	16.0	−16.0
58.	225	0.0200	–	0.55	0.67	1.11	80.0	−18.3
59.	1337	0.0077	–	0.54	3.88	3.83	30.8	−17.7
60.	59	0.0022	–	0.42	1.82	2.29	8.8	−17.2
61.	1341	0.0036	–	0.44	2.44	6.43	14.4	−17.9
62.	234	0.0070	–	<0.30	0.93	2.36	28.0	−16.0
63.	784	0.0091	–	<0.27	0.89	1.38	36.4	−17.7
64.	449	0.0040	–	0.27	2.27	4.03	16.0	−17.8
65.	1346	0.0037	–	0.25	0.88	1.58	14.8	−17.4
66.	1484	0.0089	–	0.70	0.92	1.74	35.6	−17.5
67.	1363	0.0175	–	0.38	1.18	3.26	70.0	−18.0
68.	829	0.0042	–	<0.25	0.71	1.40	16.8	−17.2
69.	294	0.0080	–	<0.56	0.46	0.95	32.0	−17.7
70.	527	0.0028	–	0.49	4.37	7.19	11.2	−16.1
71.	931	0 0079	–	<0.53	0.94	2.23	31.6	−16.3
72.	400	0.0080	–	<0.31	1.22	2.32	32.0	−18.5
73.	401	0.0060	–	0.62	2.49	3.67	24.0	−18.6
74.	1235	0.0153	–	0.25	1.05	2.57	61.2	−18.9
75.	708	0.0059	0.37	0.77	5.37	7.99	23.6	−18.2
76.	1236	0.0055	–	0.32	2.28	4.85	22.0	−18.6
77.	630	0.0115	–	<0.32	0.79	1.71	46.0	−19.0
78.	33	0.0047	–	0.97	4.73	5.25	–	−18.5
79.	150	0.0130	–	0.25	0.68	1.00	52.0	−18.9
80.	35	0.0034	0.25	0.92	5.13	6.37	–	−18.1
81.	418	0.0056	–	<0.25	1.74	3.02	22.4	−18.8
82.	197	0.0080	–	<0.25	0.57	1.01	32.0	−18.1
83.	1466	0.0038	–	1.21	5.88	10.60	15.2	−18.9
84.	439	0.0035	0.34	0.72	5.91	11.20	14.0	−18.7
85.	52	0.0068	0.35	1.09	4.58	5.91	27.2	−19.0
86.	225	0.0200	–	0.55	0.67	1.11	80.0	−18.3
87.	53	0.0160	–	<0.26	0.63	1.61	64.0	−18.8
88.	1344	0.0099	–	0.99	2.89	2.63	39.6	−18.8
89.	245	0.0200	–	<0.25	0.41	1.02	80.0	−18.8
90.	1348	0.0241	–	0.25	0.80	1.55	96.4	−18.8
91.	267	0.0120	0.89	0.25	1.14	1.86	48.0	−18.4
92.	802	0.0141	–	<0.38	0.66	1.01	56.4	−18.9
93.	803	0.0138	–	<0.35	0.45	1.70	55.2	−18.8
94.	1379	0.0088	0.28	0.80	4.73	6.87	35.2	−19.0
95.	685	0.0152	–	<0.25	0.86	1.09	60.8	−19.0
96.	852	0.0216	–	0.25	1.07	2.03	86.4	−18.8
97.	482	0.0119	–	<0.25	0.84	1.56	47.6	−18.9
98.	490	0.0095	–	<0.25	0.64	1.32	38.0	−18.2
99.	1496	0.0074	–	<0.25	0.66	1.23	29.6	−18.2
100.	296	0.0160	–	<0.25	0.55	1.30	64.0	−18.9
101.	500	0.0265	–	<0.25	1.25	2.60	106.0	−19.0
102.	1121	0.0157	–	<0.25	0.70	1.22	62.8	−18.6
103.	513	0.0180	–	<0.25	0.81	1.48	72.0	−18.7
104.	899	0.0185	–	<0.30	0.73	1.63	74.0	−18.7
105.	908	0.0040	–	<0.25	0.88	1.90	16.0	−18.1
106.	912	0.0166	–	<0.25	1.51	3.03	66.4	−18.9
107.	1124	0.0169	–	<0.34	0.50	1.96	67.6	−18.4
108.	314	0.0078	–	<0.25	1.29	1.55	31.2	−18.8
109.	317	0.0210	–	<0.25	0.66	1.25	84.0	−19.0

Table 3 The sample of HII galaxies (de Grijp *et al.* (1987)) based on IRAS catalogue and spectral observations

1	*Object* 2	z 3	S_{12} 4	S_{25} 5	S_{60} 6	S_{100} 7	V_{mag} 8
1.	IRAS0002 − 084	0.0301	0.22	0.42	1.40	1.57	15.9
2.	IRAS0026 − 102E	0.0496	0.16	0.51	1.07	0.97	15.8
3.	IRAS0032 − 617SW	0.0286	0.12	0.16	1.16	2.03	14.8
4.	IRAS0034 − 338	0.0205	0.43	2.52	6.71	4.53	13.8
5.	IRAS0038 + 235W	0.0852	0.07	0.14	0.77	0.91	17.1
6.	IRAS0046 − 127	0.0288	0.11	0.23	1.36	1.97	14.4
7.	IRAS0105 + 331	0.0155	0.07	0.17	0.67	1.06	13.5
8.	IRAS0207 − 104	0.0127	0.58	2.21	12.17	18.13	12.6
9.	IRAS0225 − 103E	0.0068	0.11	0.36	1.50	1.91	13.2
10.	IRAS0229 + 025	0.0272	0.09	0.20	0.62	1.11	15.5
11.	IRAS0302 − 472	0.0305	0.09	0.25	0.90	1.81	13.9
12.	IRAS0330 − 623	0.0280	0.06	0.36	0.78	1.02	14.9
13.	IRAS0334 − 210	0.0058	0.45	1.93	7.12	5.71	12.1
14.	IRAS0433 + 021	0.0116	0.27	0.99	3.61	3.81	14.3
15.	IRAS0524 − 192	0.0280	0.10	1.11	1.47	1.02	13.0
16.	IRAS0751 + 534	0.0248	0.13	0.20	1.37	3.24	13.4
17.	IRAS0943 + 032N	0.0202	0.48	0.58	5.19	11.32	13.8
18.	IRAS0945 + 594	0.0072	0.09	0.23	0.89	1.20	13.4
19.	IRAS1045 + 503	0.0229	0.20	0.33	0.58	1.32	14.0
20.	IRAS1119 + 045	0.0378	0.88	0.49	0.84	2.15	15.2
21.	IRAS1131 + 216	0.0214	0.17	0.22	1.00	2.38	12.9
22.	IRAS1215 + 064	0.0184	0.22	0.86	2.72	3.11	13.4
23.	IRAS1223 − 388	0.0120	0.09	0.26	1.13	2.66	13.2
24.	IRAS1231 + 779SE	0.0277	0.08	0.12	0.89	1.97	14.2
25.	IRAS1324 + 268W	0.0234	0.14	0.24	0.71	0.71	14.1
26.	IRAS1337 − 313	0.0009	2.59	12.21	30.91	29.04	9.9
27.	IRAS1407 + 266	0.0597	0.07	0.07	0.89	1.13	15.5
28.	IRAS1428 − 030	0.0428	0.13	0.17	0.77	1.60	17.0
29.	IRAS1442 + 590	0.0388	0.12	0.11	0.75	1.66	14.8
30.	IRAS1506 + 661	0.0286	0.15	0.16	1.80	3.51	13.9
31.	IRAS1531 + 580S	0.0391	0.13	0.24	1.10	1.39	15.2
32.	IRAS1559 + 832	0.0216	1.26	0.44	0.76	1.18	14.7
33.	IRAS1657 + 290	0.0322	0.18	0.13	1.07	2.42	13.1
34.	IRAS1716 + 302NE	0.0140	0.07	0.25	0.92	1.00	14.2
35.	IRAS1743 + 579S	0.0386	0.06	0.14	0.77	0.77	15.6
36.	IRAS1908 − 539NW	0.0230	0.18	0.36	1.45	4.10	13.6
37.	IRAS1918 − 558	0.0120	0.09	0.18	0.54	1.71	12.9
38.	IRAS1926 − 425E	0.0596	0.09	0.11	1.10	2.02	16.4
39.	IRAS1926 − 436E	0.0597	0.36	0.53	0.71	1.04	15.8
40	IRAS2002 − 204NW	0.0687	0.20	0.22	0.20	0.60	16.9
41.	IRAS2116 − 206	0.0390	0.10	0.57	1.81	2.31	14.3
42.	IRAS2117 − 492W	0.0541	0.10	0.13	0.73	1.22	15.7
43.	IRAS2226 − 659	0.0106	0.24	0.48	1.74	3.67	12.5
44.	IRAS2311 − 578E	0.0348	0.10	0.13	0.71	1.14	15.0
45.	IRAS2339 − 044	0.0188	0.14	0.39	2.00	3.40	13.8
46.	IRAS2346 + 019	0.0304	0.32	0.57	1.66	2.69	14.6
47.	IRAS2357 + 397W	0.0828	0.10	0.30	0.44	0.26	17.2
48.	IRAS2358 − 012	0.0854	0.09	0.52	0.67	0.98	17.6

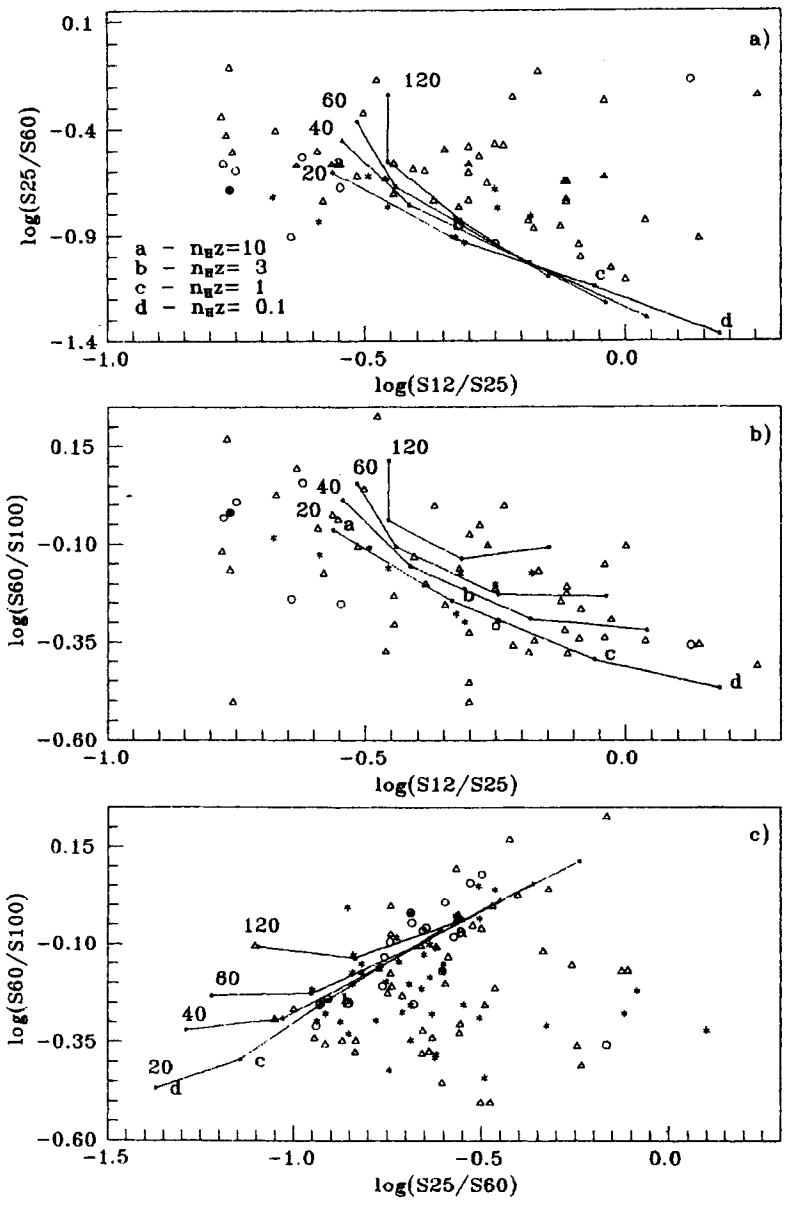

Figure 3 Relation between FIR colors of the SFRs having $M_{tot} = 1 \times 10^6\,\mathfrak{M}_\odot$ for various values of the upper mass cutoff and different choices of $n_H z$ (given in Figure 3a.) For the sake of comparison, the HII galaxies from de Grijp *et al.* (1987) selected from the IRAS catalog (triangles), low-luminosity Markarian galaxies from Markarian *et al.* (1989) (asterisks) and BCDGs from Kunth and Sevre (1985) and Klein *et al.* (1984) (circles) are also given.

to assume that the value of **X**, which determines the proportion between the dust grains and PAH molecules number densities, should differ substantially from one galaxy to another (see below). Thus, colors of the bulk of the blue compact dwarf galaxies and HII galaxies are successfully explained in the framework of the BCDG model consisting of an isolated star forming region. The color diagrams are affected only weakly by both the upper stellar mass cutoff m_u in the central energy source and the slope of the initial mass function (Figure 4).

Figure 5 shows the FIR color diagrams for star forming regions with different total stellar masses $M_{\rm tot} = 10^5\,\mathfrak{M}_\odot$–$10^7\,\mathfrak{M}_\odot$. The model with $M_{\rm tot} = 10^5\,\mathfrak{M}_\odot$ is inconsistent with the observed colors. The SFR models with $M_{\rm tot} = 10^6$–$10^7\,\mathfrak{M}_\odot$ and $n_{\rm H}z = 1$–3 show the best agreement with observational data for the BCDGs. As follows from observations, the ionized hydrogen mass in the BCDGs exceeds $10^6\,\mathfrak{M}_\odot$ and the mean value of the number density is about $10\,{\rm cm}^{-3}$. When the deficiency of the heavy elements has been taken into account, one can evaluate the values of $n_{\rm H}z$ given above. The models with $n_{\rm H}z > 1$–3 are inadequate because absorption in the **B** band in this case becomes substantial, which is not confirmed by spectral observations in the visible range. The typical observed value of extinction $\mathbf{A}_{\rm v}$ in the ionized hydrogen regions in the BCDGs is less than 1^m which is consistent with the model value $n_{\rm H}z < 1$–3.

As already noted above, PAH molecules can contribute substantially to the galaxy emission at $\lambda = 12\,\mu$m. To assess the effect of PAH molecules, we performed the SFR model calculations with different **X** values. Color diagrams for models with $M_{\rm tot} = 10^6\,\mathfrak{M}_\odot$, $m_u = 60\,\mathfrak{M}_\odot$ and several values of **X** are given in Figure 6. The value of **X** varies from 0.17 to 1. It is the proper choice of **X** which allows us to fit the colors observed on the diagram $\log(S_{25}/S_{60})$ vs. $\log(S_{12}/S_{25})$.

The models have to explain not only the colors but also the total fluxes observed in the far infrared range. For the predicted and observed values to be compared, all quantities have been calculated for the distance of 1 Mpc.

Figure 7 shows S_{60}, the monochromatic luminosity at $\lambda = 60\,\mu$m, (S_{60} is measured in units of Jy × Mpc^{-2}) vs. $\log(S_{60}/S_{100})$, $\log(S_{12}/S_{25})$ and $\log(S_{25}/S_{60})$ for the models with $M_{\rm tot} = 10^6\,\mathfrak{M}_\odot$, $\mathbf{X} = 0.63$ and $m_u = 20$, 40, 60 and $120\,\mathfrak{M}_\odot$. In contrast to the color diagrams, where we obtained a satisfactory agreement between observed and predicted values for the most galaxies, in Figure 7 the galaxies tend to have monochromatic luminosities substantially larger than those predicted by our SFR models. There are probably some reasons for such differences. For instance, a galaxy may contain not only one but several (tens) star forming regions; a significant contribution to the FIR emission can be made not only by SFRs but also by the old stellar population. These are the cases which will be considered below.

Figure 8 shows the plots of S_{60} vs. $\log(S_{12}/S_{25})$, S_{60} vs. $\log(S_{25}/S_{60})$, and S_{60} vs. $\log(S_{60}/S_{100})$ for a fixed upper mass cutoff $m_u = 60\,\mathfrak{M}_\odot$ and several choices of the total mass, $M_{\rm tot} = 1\times10^5\,\mathfrak{M}_\odot$, $1\times10^6\,\mathfrak{M}_\odot$ and $1\times10^7\,\mathfrak{M}_\odot$, and $n_{\rm H}z = 0.1$–10. As follows from Figure 8, the luminosities of BCDGs (circles) and low-luminosity Markarian galaxies (asterisks) are best accounted for with the models consisting of one or several star forming regions, each having the total stellar mass of about $M_{\rm tot} = 10^6\,\mathfrak{M}_\odot$. At the same time, the HII galaxies (triangles) selected on the basis of the IRAS data, have luminosities substantially larger than predicted. Such luminosities cannot be accounted for by the model or a combination of the SFR models proposed for the BCDGs. To explain the color $\log(S_{60}/S_{100})$ in HII

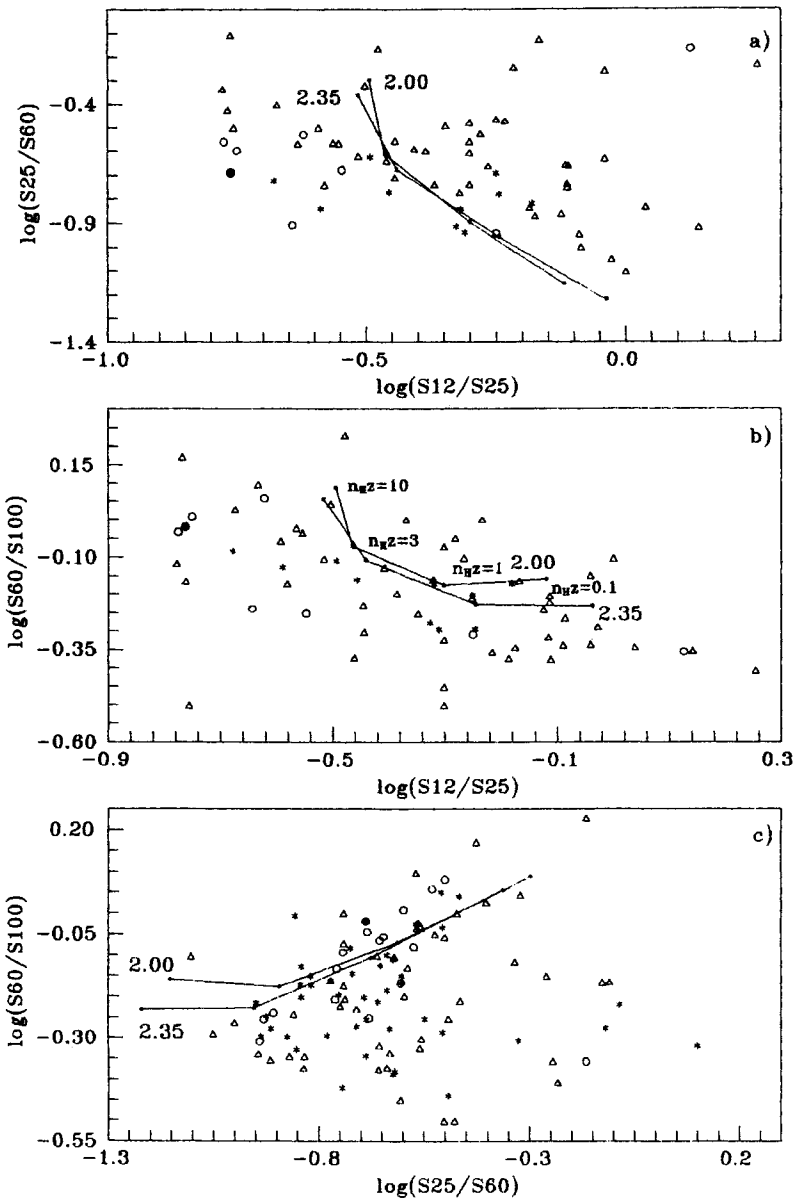

Figure 4 Relation between FIR colors of the SFRs with different slopes of the initial mass function. Notations are the same as in Figure 3.

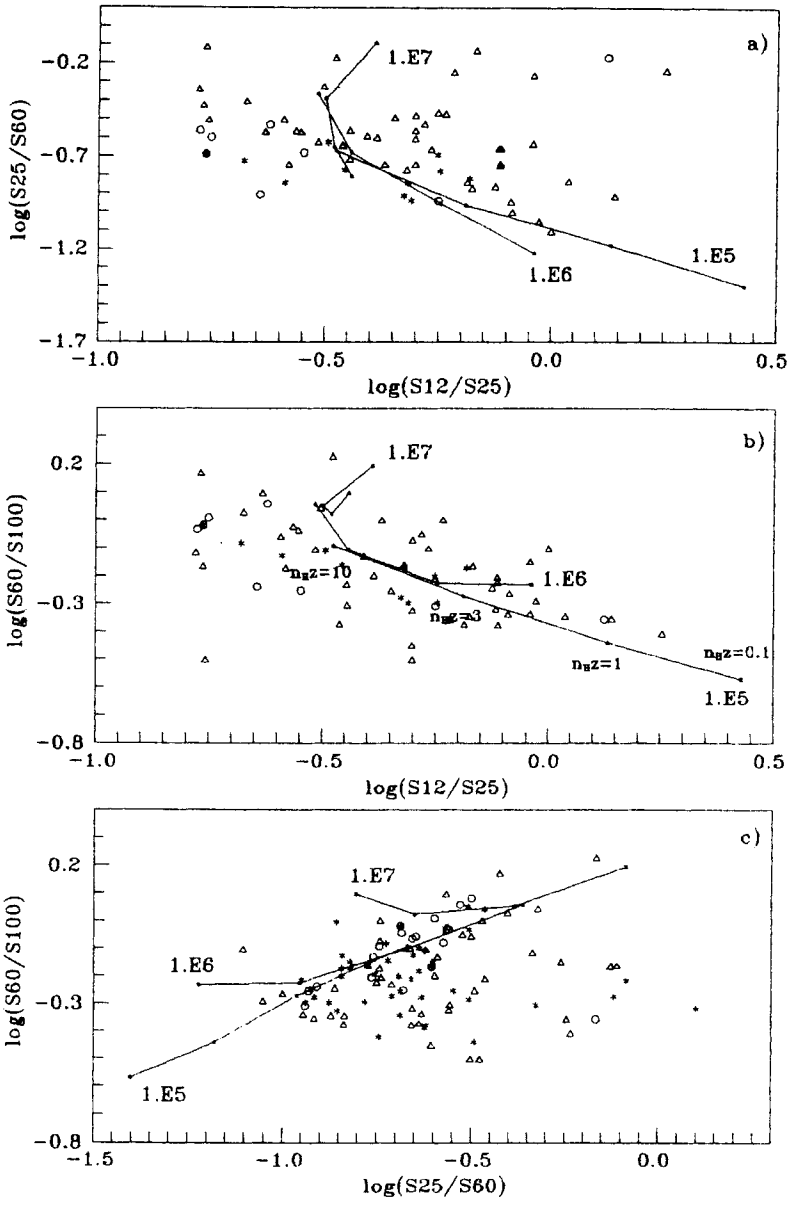

Figure 5 Relation between FIR colors of the SFRs with different choices of $M_{\rm tot} = 1 \times 10^5\,\mathfrak{M}_\odot$–$1 \times 10^7\,\mathfrak{M}_\odot$ and $n_{\rm H}z$. Notations are as those in Figure 3.

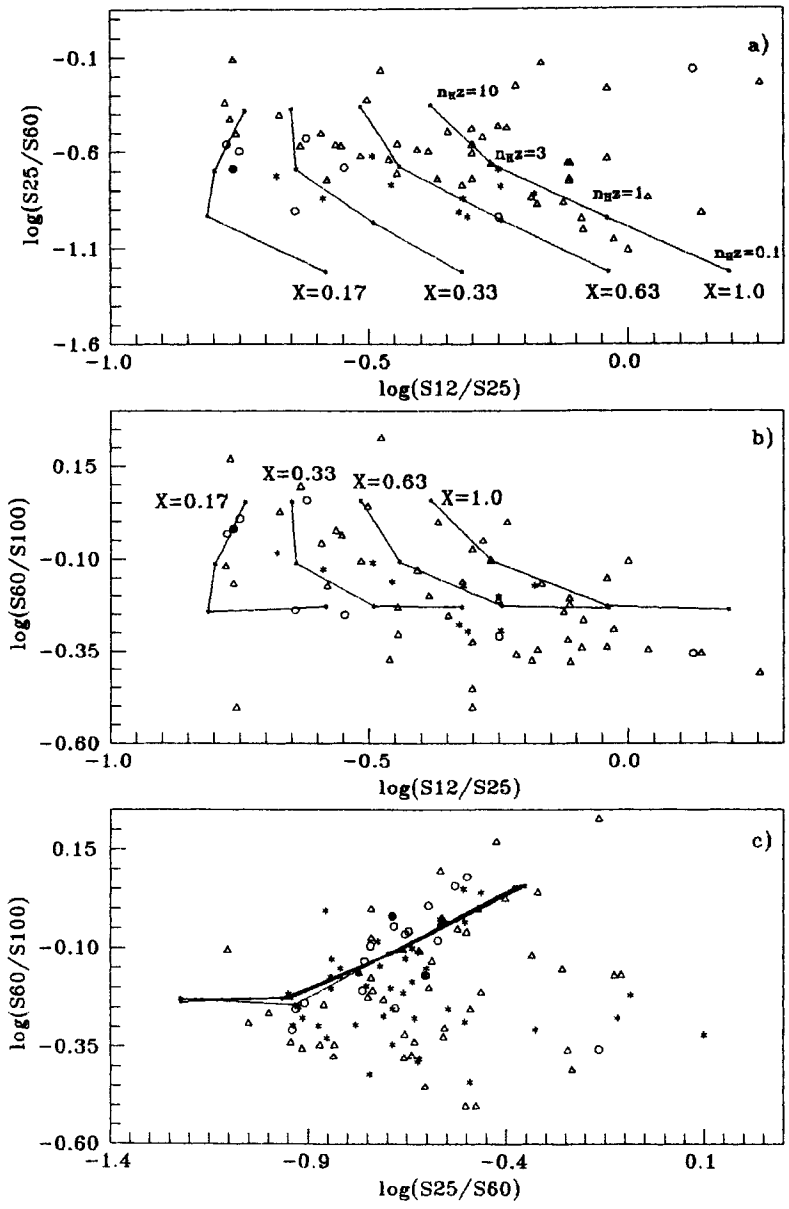

Figure 6 Relation between FIR colors of the SFRs for $M_{\text{tot}} = 1 \times 10^6\,\mathfrak{M}_\odot$, $m_u = 60\,\mathfrak{M}_\odot$ and several values of the PAH molecules abundance $\mathbf{X} = 0.17$–1.0. Notations are the same as in Figure 3.

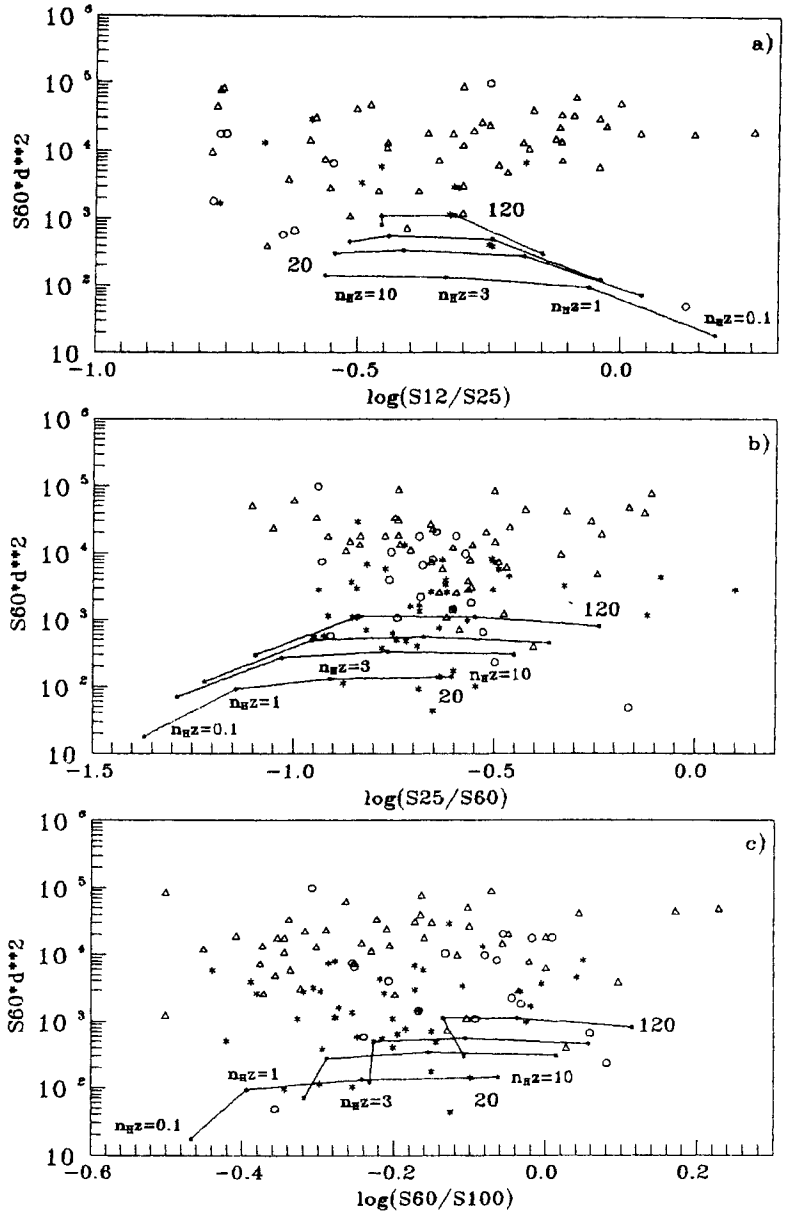

Figure 7 Relation between the monochromatic luminosity S_{60} at $\lambda = 60\,\mu$m and FIR colors of the SFRs for $M_{\rm tot} = 1 \times 10^6\,\mathfrak{M}_\odot$, $\mathbf{X} = 0.63$ and $m_u = 20, 40, 60, 100\,\mathfrak{M}_\odot$. Notations are the same as in Figure 3.

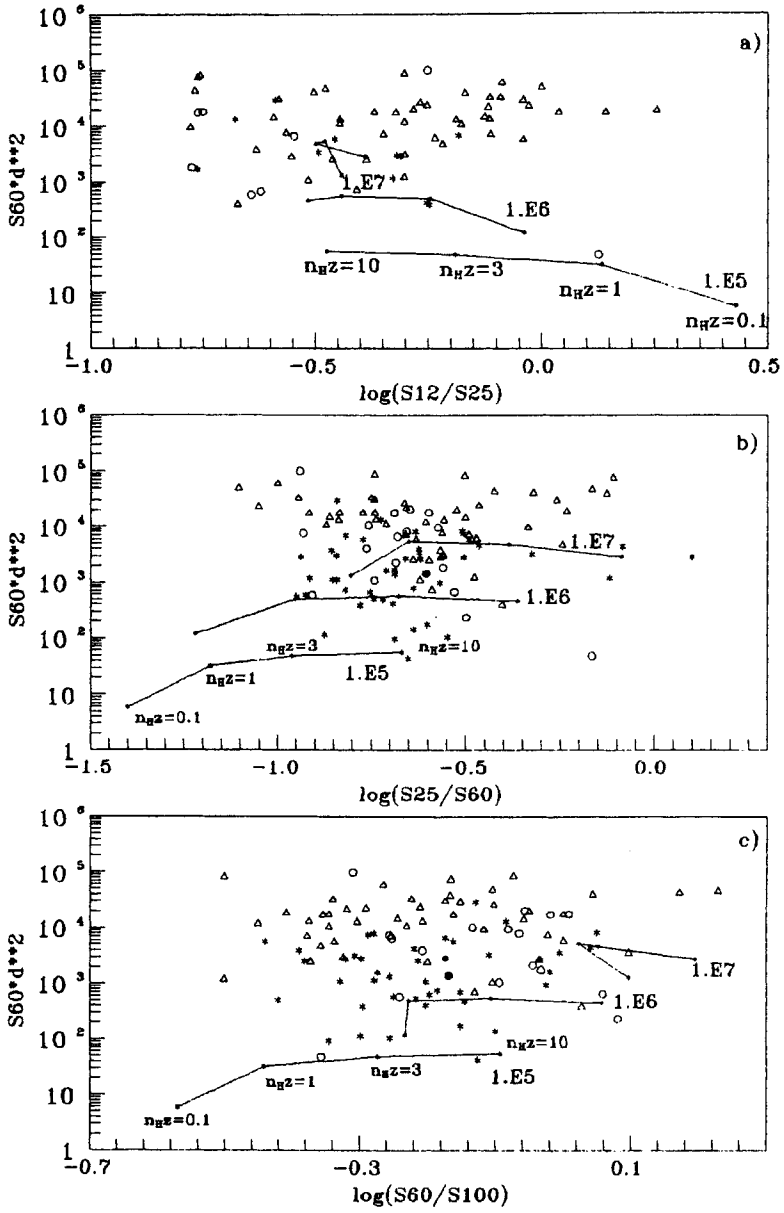

Figure 8 Relation between the monochromatic luminosity S_{60} at $\lambda = 60\,\mu$m and FIR colors of the SFRs for a fixed upper mass cutoff $m_u = 60\,\mathfrak{M}_\odot$ and several values of M_{tot} and $n_H z$. Notations are the same as in Figure 3.

galaxies observed by de Grijp *et al.* (1987), the presence of a large amount of dust grains heated only to $T_d \sim 10$–20 K which emit only in the 100 μm band should be assumed. This conclusion is also true for low-luminosity Markarian galaxies which have $\log(S_{60}/S_{100}) < -0.2$. Varying the value of **X** which defines the proportion between the dust grains and PAH molecules, we obtain a satisfactory agreement between the observed and predicted values of the color $\log(S_{12}/S_{25})$ in the framework of the model of uniform-density SFRs (Figure 9).

3.3. *A Model Including Several Star Forming Regions with Different Densities*

In order to explain properties of the galaxies in the far infrared range, Leech *et al.* (1989) proposed a combined model which includes several star forming regions. In this model, dense star forming regions unobservable in the visible range consistently explain the galaxy color characteristics in the FIR range. The star forming regions having smaller densities, which are readily observable in the visible range, give suitable values of L_{FIR}/L_B for some BCDGs. A sufficiently high value of the far infrared luminosity is achieved by a suitable choice of the number of the star forming regions.

Figure 10 shows the colors for the galaxy models consisting of dense (d) and rarefied (r) star forming regions. As follows from Figure 10, the models which combine the dense star forming regions with $n_H z = 1.0$ and rarefied ones with $n_H z = 0.01$ are consistent enough. In these models, the number of the rarefied star forming regions is about ~5–10 times as large as the number of the dense ones. Taking into account that heavy element abundance for the BCDGs is about ~10 times as small as the solar one (Coleman *et al.* (1980)), one can infer the star forming region densities to be about 10 cm^{-3} (dense) and 0.1 cm^{-3} (rarefied). The typical value $L_{FIR}/L_B \sim 10$–15 explains the far infrared properties of the some galaxies in the FIR range. But the mean value of L_{FIR}/L_B for observed BCDGs is about 2–3 times below that predicted by the models, and a combination of star forming regions cannot help in explaining the mean value of L_{FIR}/L_B. Moreover, the model combined from dense and rarefied star forming regions of uniform densities cannot account satisfactorily for the observed values of the colors $\log(S_{25}/S_{60})$.

3.4. *Models of Inhomogeneous Star Formation Regions*

To obtain correct values of $\log(S_{25}/S_{60})$, the star forming region should be assumed to be inhomogeneous having the gradient of $n_H z$ due to increasing gas density and relative dust grain abundance towards the galaxy center. In this case inner SFR layers (being more dense) contribute substantially in the emission at $\lambda = 25$ μm. Emission at $\lambda = 60$ μm and $\lambda = 100$ μm is generated in the outer SFR layers (which are more rarefied). The model parameters have been chosen in such way that the optical depth at $\lambda = 5500$ Å falls into the range $\tau = 0$–2, which is consistent with the observed data for the ionized hydrogen region in the BCDGs. In this model the SFR is taken to consist of several nested spherical homogeneous shells. Each shell has its own density distinct from that in another part. For the Sobolev (1960) analytic solution of the transfer equation to be applicable, the inner radius of each shell has been taken to be substantially smaller than that for

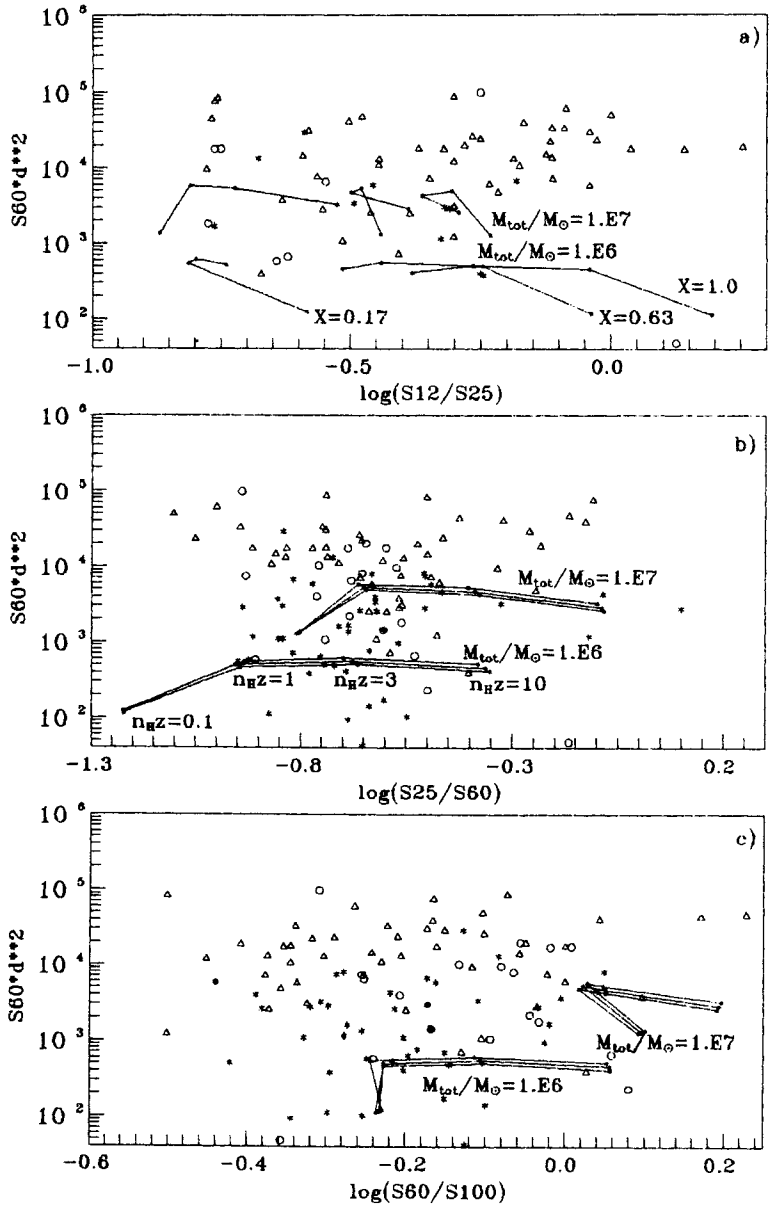

Figure 9 Relation between FIR colors of the SFRs for various values of M_{tot} and **X**. Notations are the same as in Figure 3.

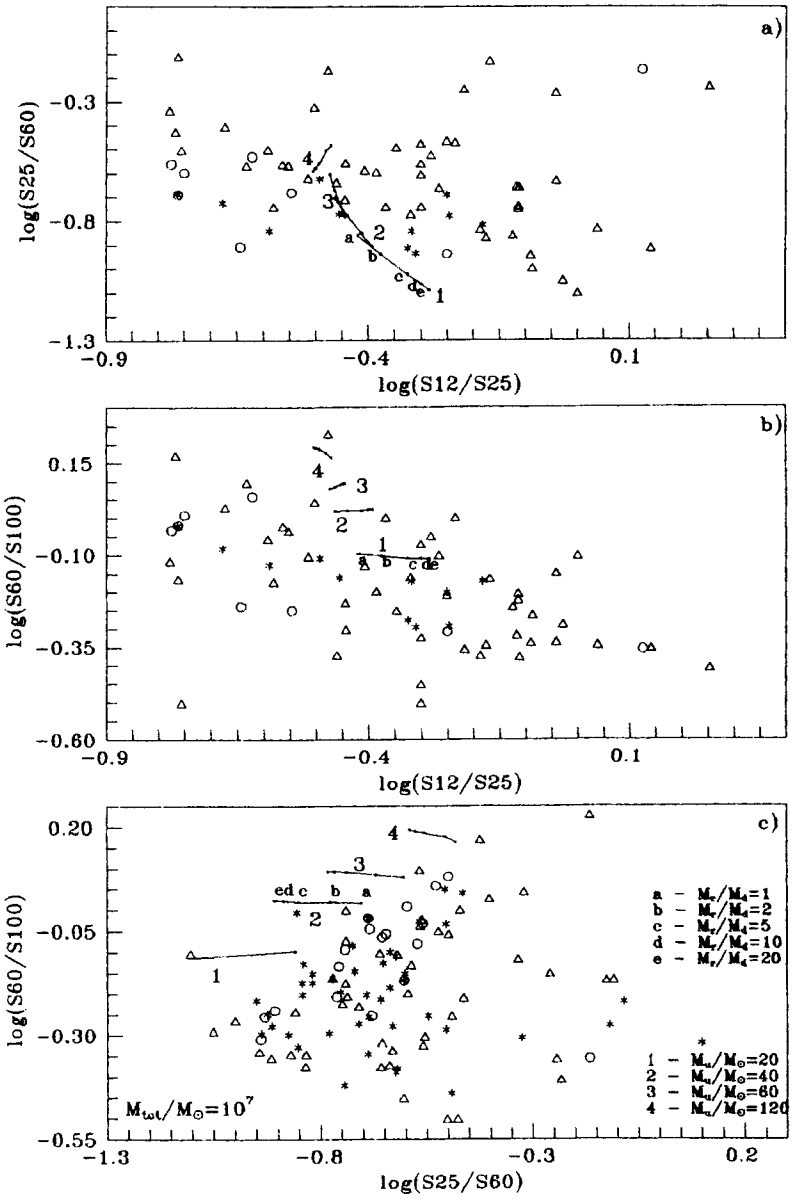

Figure 10 The FIR color diagram for combined models consisting of dense and rarefied SFRs. Notations are the same as in Figure 3.

the next outer one. Then the emission propagating from any spherical shell can be considered as being a point-like source for the next outer shell.

In the present paper, three models of the star forming region which consists of three shells with external radii 1×10^{20} cm, 2×10^{21} cm and 6.17×10^{21} cm, respectively, have been studied. The chosen values of $n_H z$ are as follows: model I: $n_H z = 1.0$, 0.3, 0.03 and $\mathbf{A}_v = 0.15$; model II: $n_H z = 3.0$, 1.0, 0.1 and $\mathbf{A}_v = 0.49$; model III: $n_H z = 10.0$, 3.0, 0.1 and $\mathbf{A}_v = 1.21$.

Figure 11 shows the FIR color diagram for the inhomogeneous SFR with the fixed set of $n_H z$ (1.0, 0.3 and 0.03) and $M_{tot} = 1 \times 10^5\, \mathfrak{M}_\odot$, $1 \times 10^6\, \mathfrak{M}_\odot$ and $1 \times 10^7\, \mathfrak{M}_\odot$ with the upper mass cutoff for the central stellar cluster $m_u = 20$–$120\, \mathfrak{M}_\odot$. The model of inhomogeneous SFR consistently explains the position of the BCDGs (circles) in the colors diagram. In particular, the predicted and observed colors $\log(S_{60}/S_{100})$ vs. $\log(S_{25}/S_{60})$ agree much better than above. Moreover, the FIR color characteristics of the SFR turn out to be only weakly dependent on $n_H z$. The calculations show that the curves corresponding to $n_H z = 1.0$, 0.3 and 0.03 almost exactly coincide with those for $n_H z = 3.0$, 1.0 and 0.1. For the models with inhomogeneous SFR the FIR colors turn out to depend stronger on M_{tot} and on m_u.

In all the models examined above, the star forming regions provide the main contribution into the galaxy emission in the far infrared range. All these models cannot explain the position of a large number of Markarian galaxies and HII galaxies in the color diagrams (note for instance the points in the right lower corner in Figure 11c). The presence of a "cold" dust heated by the old stellar population should be assumed for these galaxies. The colors of the BCDGs are then consistently explained within the framework of the inhomogeneous SFR model. But the ratio of L_{FIR}, the luminosity in the far infrared range, to L_B, the luminosity in the visible range, for the BCDGs is as a rule smaller than that obtained in the framework of the models discussed above. Therefore, the assumption about the presence of the old stellar population is a good idea also in the case of the BCDGs. But, in contrast to low-luminosity Markarian galaxies and HII galaxies, in the case of the BCDGs the old stellar population contributes only to the luminosity in the visible range.

3.5 *Models with a "Cold" Dust Component*

As noted above, the old stellar population is detected in the bulk of the blue compact dwarf galaxies through near-infrared observations. This population originates probably in earlier starbursts (Kunth *et al.*, 1988). This underlying old stellar population can heat the dust grains up to the temperatures $T_d \sim 25$–30 K and in such way contributes to the far infrared galaxy emission in the 60 μm and mostly 100 μm bands. In the present paper, the distribution of the old stars in the BCDGs is assumed to be similar to that in an elliptical galaxy (see section 2) with the radius $R = 2$ kpc or $R = 5$ kpc. In Table 4 the FIR colors and other characteristics of the underlying elliptical galaxy are given. So far as the BCDGs color characteristics are consistently explained with the models of the SFR, the conclusion about negligible contribution of the old stellar population to the FIR emission is plausible, while the elliptical galaxy can contribute substantially into the L_B luminosity. With this contribution taken into account, the ratio L_{FIR}/L_B decreases down to the values observed.

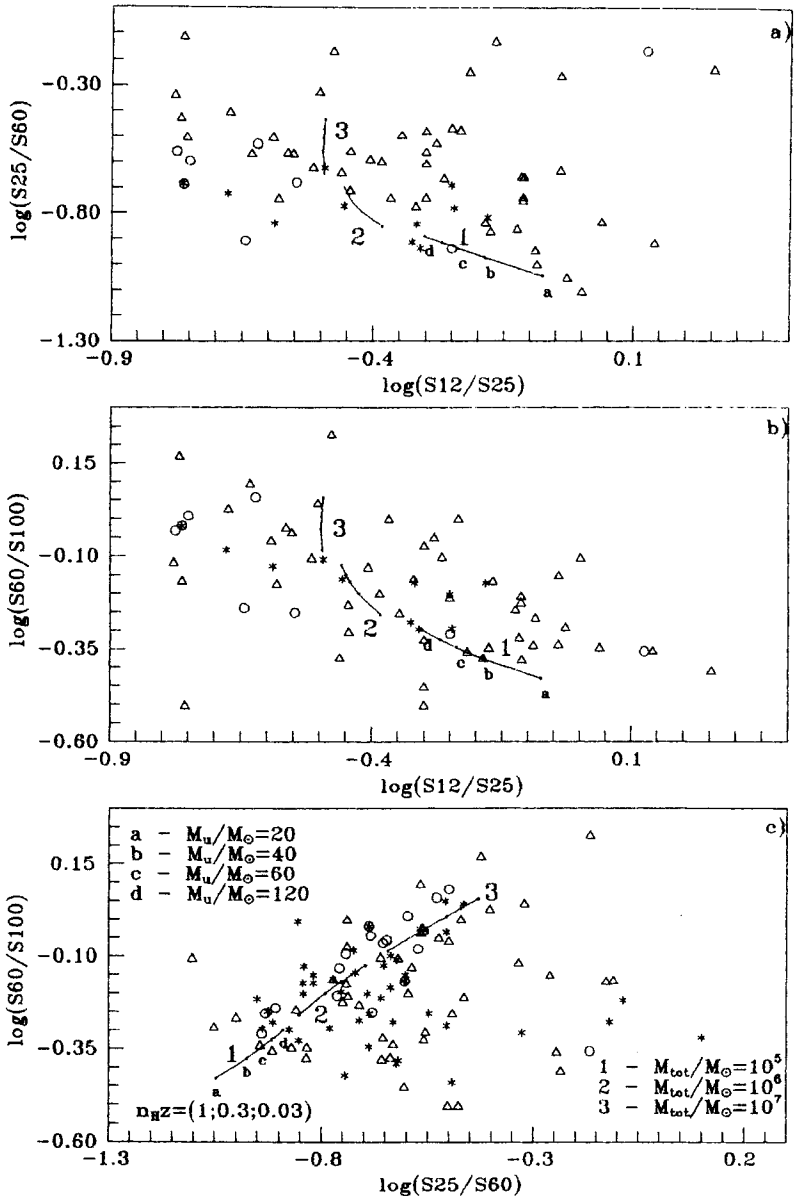

Figure 11 The FIR color diagram for the models of inhomogeneous SFR with $n_H z = (1.0, 0.3, 0.03)$, $M_{tot} = 1 \times 10^5 \mathfrak{M}_\odot - 1 \times 10^7 \mathfrak{M}_\odot$ and several choices of $m_u = 20-120\,\mathfrak{M}_\odot$. Notations are the same as in Figure 3.

Table 4 Models for the underlying elliptical galaxy

	$R = 1\ kpc$		$R = 2\ kpc$		$R = 5\ kpc$	
M_{tot}	$10^7\ \mathfrak{M}_\odot$	$10^8\ \mathfrak{M}_\odot$	$10^7\ \mathfrak{M}_\odot$	$10^8\ \mathfrak{M}_\odot$	$10^7\ \mathfrak{M}_\odot$	$10^8\ \mathfrak{M}_\odot$
$L_B/L_\odot$	$8.31\ 10^6$	$8.31\ 10^6$	$6.65\ 10^7$	$6.65\ 10^7$	$1.04\ 10^9$	$1.04\ 10^9$
					$1.04\ 10^9$	$1.04\ 10^9$
$L_{FIR}/L_\odot$	$2.96\ 10^7$	$2.96\ 10^8$	$6.98\ 10^7$	$6.98\ 10^8$	$1.99\ 10^8$	$1.99\ 10^9$
					$3.60\ 10^8$	$3.60\ 10^9$
S_{12} (Jy)	0.06	0.61	0.12	1.22	0.31	3.05
					0.52	5.26
S_{25} (Jy)	$3.29\ 10^{-3}$	$3.29\ 10^{-2}$	0.03	0.34	0.51	5.06
					1.35	13.46
S_{60} (Jy)	$1.11\ 10^1$	$1.11\ 10^2$	$3.25\ 10^1$	$3.25\ 10^2$	$1.15\ 10^2$	$1.15\ 10^3$
					$2.25\ 10^2$	$2.25\ 10^3$
S_{100} (Jy)	$4.75\ 10^1$	$4.75\ 10^2$	$9.56\ 10^1$	$9.56\ 10^2$	$2.17\ 10^2$	$2.17\ 10^3$
					$3.47\ 10^2$	$3.47\ 10^3$

Notes: In the first line the model results with $n_H = n_H^0(r/r_0)^2$ are shown for each parameter, in the second line, those with $n_H = n_H^0(r/r_0)^3$. The value of z is taken to be unity.

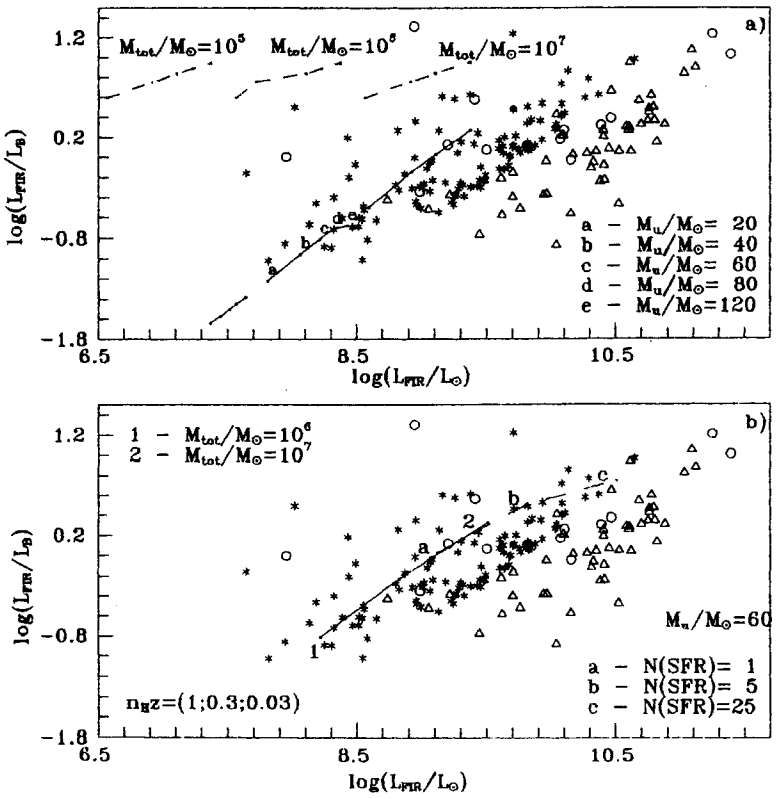

Figure 12 (*a*) L_{FIR}/L_B vs. L_{FIR} for the models consisting of an underlying elliptic galaxy ($R = 5$ kpc, $M_{GAL} = 1 \times 10^7\ \mathfrak{M}_\odot$, $n_H z = 0.1$) and SFRs with $M_{tot} = 1 \times 10^5\ \mathfrak{M}_\odot$–$1 \times 10^7\ \mathfrak{M}_\odot$ and $m_u = 20$–$120\ \mathfrak{M}_\odot$ (full lines). The curves for the models which consist only of a single SFR without the elliptic galaxy are shown dashed. (*b*) L_{FIR}/L_B vs. L_{FIR} for models which consist of an underlying elliptic galaxy as in Figure 12a and several SFRs with their number indicated with $M_{tot} = 1 \times 10^6\ \mathfrak{M}_\odot$ and $m_u = 60\ \mathfrak{M}_\odot$. Notations are the same as in Figure 3.

Figure 12a shows the far infrared excess, L_{FIR}/L_B vs. L_{FIR}, for the galaxies studied in the present paper. Results of the model calculations for a single inhomogeneous star forming region with an underlying elliptical galaxy ($R =$ 5 kpc) are also shown given in this figure (full lines). For the underlying elliptical galaxy, we take $M_{HI} = 10^7\,\mathfrak{M}_\odot$ and $n_H z = 0.1$. The star forming regions have $M_{tot} = 10^5$–$10^7\,\mathfrak{M}_\odot$ and the upper mass cutoff $m_u = 20$–$120\,\mathfrak{M}_\odot$. Dependences L_{FIR}/L_B vs. L_{FIR} for the models which consist only of isolated SFRs without the underlying elliptical galaxy are shown by dashed lines. The position of the BCDGs and Markarian galaxies with low L_{FIR} is consistently explained by the combined model (SFR + underlying elliptical galaxy). The galaxy model which consists of star forming regions without underlying galaxy consistently explains the FIR excess L_{FIR}/L_B for those BCDGs which have high luminosities in the far infrared range. But the luminosity L_{FIR} itself for the SFRs alone is substantially lower than that observed. This provides a strong evidence that the BCDGs with large L_{FIR} include a large number of SFRs of the total mass of, probably, $M_{tot} = 10^6$–$10^7\,\mathfrak{M}_\odot$. Both L_{FIR} and L_B are produced only by SFRs in these galaxies.

In Figure 12b we plot L_{FIR}/L_B vs. L_{FIR} for galaxy models which consist of the underlying elliptical galaxy with the same parameters as in Figure 12a and several SFRs. The numbers displayed in Figure 12b give the number of the SFRs. The models with the star forming regions having $M_{tot} = 10^6\,\mathfrak{M}_\odot$ and $m_u = 60\,\mathfrak{M}_\odot$ are shown using full lines, those with the SFRs of $M_{tot} = 10^7\,\mathfrak{M}_\odot$ and $m_u = 60\,\mathfrak{M}_\odot$ are shown using dashed lines. The set of such models consistently explains the position of the BCDGs and most of the low-luminosity Markarian galaxies in the L_{FIR}/L_B vs. L_{FIR} diagram. But the combined models (SFRs + underlying elliptical galaxy) are inadequate in the case of the HII galaxies from the sample of de Grijp *et al.* (1987) and some Markarian galaxies in this diagram. To explain positions of these galaxies in the color and L_{FIR}/L_B vs. L_{FIR} diagrams, an underlying disk component probably has to be included in the models along with the SFRs.

4. CONCLUSIONS

We have presented the main results of the simulation of the blue compact dwarf galaxies emission in the far-infrared range. Our principal conclusions are as follows:

1. On the basis of the analytic solution of Sobolev (1960) for the radiation transfer equation, a set of numerical codes has been constructed which allows to simulate radiation transfer in a homogeneous, uniform, spherically symmetric cloud. A star cluster of the total mass $M_{tot} = 10^5\,\mathfrak{M}_\odot$–$10^7\,\mathfrak{M}_\odot$, the upper mass cutoff $m_u = 20\,\mathfrak{M}_\odot$–$120\,\mathfrak{M}_\odot$ and with different slopes of the IMF has been taken as a central energy source. The models have been constructed with due regard for the size distribution of dust grains and for the presence of polycyclic aromatic hydrocarbon (PAH) molecules, which contribute substantially into the galaxy radiation at $\lambda = 12\,\mu$m.

As far as blue compact dwarf galaxies have no active nucleus, we allow for the following main sources of the galactic FIR radiation: the general interstellar ultraviolet radiation field produced by the galactic background stellar population and hot OB stars radiation in giant ionized hydrogen regions.

The models proposed here allow to calculate the output radiation flux in the visible range, the temperature distribution of the dust grains heated by the central energy source, the flux density at $\lambda\lambda$ 12, 25, 60 and 100 μm, and the total far-infrared luminosity $L_{\rm FIR}$.

2. The following models of the blue compact dwarf galaxies have been considered:

(*a*) The BCDG consisting of one or several (tens) homogeneous SFRs, each having its own value of $n_{\rm H}z$, $M_{\rm tot}$ and m_u.

(*b*) The BCDG consisting of dense and rarefied SFRs.

(*c*) The BCDG consisting of several (tens) inhomogeneous SFRs with different values of $n_{\rm H}z$.

(*d*) The BCDG consisting of the SFRs [one of the cases (a)–(c)] and an underlying elliptical galaxy having old stellar population ($R = 5$ kpc, $r_0 = 0.1\,R$, the total neutral hydrogen mass $M_{\rm HI} = 1 \times 10^7\,\mathfrak{M}_\odot$, and the distribution of neutral gas taken as a power-law function).

3. Comparison of our results with observations shows that:

(*a*) The "warm" dust heated up to $T \sim 40$–60 K by the hot stars of the star forming regions is the main source of far-infrared radiation in most blue compact dwarf galaxies:

(*b*) The positions of most of the BCDGs in the FIR color diagram and in $L_{\rm FIR}/L_{\rm B}$ vs. $L_{\rm FIR}$ diagram can be explained in the framework of the galaxy models combining an underlying elliptical galaxy having old stellar population and several (tens) inhomogeneous SFRs (having $n_{\rm H}z = 3.0$–0.1 and the total mass 10^6–$10^7\,\mathfrak{M}_\odot$). The star forming regions are shown to provide the dominant contribution to the FIR radiation of the BCDGs, while the old stellar population affects mainly the luminosity in the visible range.

4. The FIR characteristics of the large number of Markarian galaxies and most of HII galaxies cannot be explained consistently in the framework of the studied models (underlying elliptical galaxy + star forming regions). In order to explain the FIR characteristics of these galaxies, the model probably should include, along with SFRs, a massive disk of old stars which heat the dust up to $T_{\rm d} < 20$ K.

The authors are indebted to N. N. Fomin and E. G. Yanovitsky for useful advice.

References

Avedisova, V. S. (1979). The ionizing fluxes and the star formation rate in the Galaxy. *Astron. Zh.* **56,** 965–975.

Bruzual, G. A., Magris, G. C. and Carvet, N. (1988). A model for the effects of dust on the spectra of disk galaxies. I. General treatment. *Astrophys. J.* **333,** 673–688.

Campbell, A. W., Terlevich, R., Melnick, J. and Moles, M. (1986). The stellar populations and evolution of HII galaxies. I. High signal-to-noise optical spectroscopy. *Mon. Not. Roy. Astron. Soc.* **223,** 811–825.

Coleman, G. D., Wu, C.-C. and Weedman, D. W. (1980). Colors and magnitudes predicted for high redshift galaxies. *Astrophys. J. Suppl. Ser.* **43,** 393–416.

Crawford, G. and Rowan-Robinson, M. (1986). Models for IRAS observations of galactic HII regions. In: *Light on Dark Matter,* ed. F. P. Israel, Dordrecht, Reidel, pp. 303–304.

Dufour, R. J. and Hester, J. J. (1990). Extended emission and star formation in I Zw 18. *Astrophys. J.* **350,** 149–154.

Fanelli, M. N., O'Connel, R. W. and Thuan, T. X. (1988). Spectral synthesis in the ultraviolet. II. Stellar populations and star formation in blue compact galaxies. *Astrophys. J.* **334,** 665–687.

Fitt, A. J., Alexander, P. and Cox, M. J. (1988). A two-temperature model for the infrared and radio emission from late-type galaxies. *Mon. Not. Roy. Astron. Soc.* **233,** 907–921.

Gondhalekar, P. M., Morgan, D. H., Dopita, M. and Phillips, A. P. (1984). The nature of blue compact galaxies. *Mon. Not. Roy. Astron. Soc.* **209,** 59–67.

Grijp, de M. H. K., Miley, G. K., Keel, W. C. and Lub, J. (1987). Warm IRAS Sources. I. A catalogue of AGN candidates from the Point Source Catalog. *Astron Astrophys. Suppl. Ser.* **70,** 95–114.

Helou, G. (1986). The IRAS colors of normal galaxies. *Astrophys. J. Lett.*, **311,** L33–L36.

IRAS Catalogs and Atlases, Explanatory (1985). Washington D.C., U.S. Government Printing Office, eds. Biechman, C. A., Neugebauer, G., Habing, H. J., Clegg, P. E. and Chester, T. J.

Izotov, Yu. I., Lipovetsky, V. A., Guseva, N. G., Kniazev, A. Yu. and Stepanian, J. A. (1990). Unusually low heavy-element abundance found in blue compact dwarf galaxy SBS0335-052. *Nature.* **343,** 238–240.

Jura, M. (1982). Models for far-infrared emission from normal galaxies. *Astrophys. J.* **254,** 70–74.

Klein, U., Heidmann, J., Wielebinski, R. and Wunderlich, E. (1986). Far-infrared emission from clumpy irregular galaxies. *Astron Astrophys.* **154,** 373–375.

Klein, U., Wielebinski, R. and Thuan, T. X. (1984). Radio continuum observations of blue compact dwarf galaxies. *Astron. Astrophys.* **141,** 241–247.

Kunth, D. (1988). Dwarf galaxies. *Paris Institut d'Astrophysique Preprint* No. 250.

Kunth, D., Maurogordato, S. and Vigroux, L. (1988). CCD observations of the blue compact dwarf galaxies: a mixed bag of morphological types. *Astron. Astrophys.* **204,** 10–20.

Kunth, D. and Sargent, W. L. W. (1983). Spectrophotometry of 12 metal-poor galaxies: implications for the primordial helium abundance. *Astrophys. J.* **273,** 81–98.

Kunth, D. and Sevre, F. (1985). IRAS observations of blue compact emission line galaxies. *Paris Institut d'Astrophysique Preprint* No. 114.

Leech, K. J., Penston, M. V., Terlevich, R., Lawrence, A., Rowan-Robinson, M. and Crawford, J. (1989). High-luminosity IRAS galaxies. II. Optical spectroscopy, modelling of starburst region and comparison with structure. *Mon. Not. Roy. Astron. Soc.* **240,** 349–372.

Markarian, B. E., Lipovetsky, V. A., Stepanian, J. A., Erastova, L. K. and Shapovalova, A. I. (1989). The First Byurakan Survey. A catalogue of galaxies with UV-continuum. *Comm. Special Astrophys. Obs.* No. 62, 117 p.

Mathis, J. S., Rumpl, W. and Nordsieck, K. H. (1977). The size distribution of interstellar grains. *Astrophys. J.* **217,** 425–433.

Matteucci, F. and Tosi, M. (1985). Nitrogen and oxygen evolution in dwarf irregular galaxies. *Mon. Not. Roy. Astron. Soc.* **217,** 391–405.

O'Connell, R. W., Thuan, T. X. and Goldstein, S. J. (1978). Star formation in II Zw 70. *Astrophys. J. Lett.* **226,** L11–L15.

Phillips, M. M. and Roche, P. F. (1984). 8–13 μm spectrophotometry of galaxies. I. Galaxies with giant H II region nuclei. *Mon. Not. Roy. Astron. Soc.* **207,** 25–33.

Puget, J. L., Leger, A. and Boulanger, F. (1985). Contribution of large polycyclic aromatic molecules to the infrared emission of the interstellar medium. *Astron. Astrophys.* **142,** 19–22.

Rowan-Robinson, M. and Crawford, G. (1986). Models for IRAS galaxies. In: *Light on Dark Matter,* ed. F. P. Israel, Dordrecht, Reidel, pp. 421–424.

Sobolev, V. V. (1960). On the brightness of a spherical nebula. *Astron. Zh.* **37,** 3–8.

Sramek, R. A. and Weedman, D. (1986). Radio observations of starburst galaxies. *Astrophys J.* **302,** 640–649.

Thompson, R. I. (1984). Lyman and Balmer continuum ionization in zero-age main-sequence stars: applications to the line excess phenomenon. *Astrophys. J.* **283,** 165–168.

Xu, C. and Zotti, de G. (1989). A model for far–IR emission of non–Seyfert Markarian galaxies. *Astron. Astrophys.* **225,** 12–26.